IN THE UNITED STATES PATENT AND TRADEMARK OFFICE

In re Application of : METHOD AND SYSTEM FOR SIMULATING
SUREDA ET AL. THE DIAMETER ENLARGEMENT OF A
LESION OF A BLOOD VESSEL

Serial No. : Art Unit:

Filing Date   Herewith : Examiner:

: Date: November $\mathcal{9}$, 2001

INFORMATION DISCLOSURE STATEMENT

[x] 1.   Pursuant to 37CFR 1.97(b)
[within three months of filing or prior to first Office Action]

[ ] 2.   Certification Pursuant to 37 CFR 1.97(c)
[before Final Office Action or Allowance]

[ ] 3.   Fee Payment Pursuant to 37 CFR 1.97(c)
[before Final Office Action or Allowance]

[ ] 4.   Petition, Certification & Petition Fee Payment Pursuant to 37 CFR 1.97(d)
[before issue fee payment]

ATTN: BOX PATENT APPLICATION
Assistant Commissioner for Patents
Washington, DC 20231

Sir:

The following are submitted in the above application in compliance with 37 CFR 1.97 and
37 CFR 1.98.

[x] 5.   A list of documents on Form PTO-1449 together with copies of each identified
document and a translation thereof or a concise explanation of each non-English
language document or a Search Report or communication from a non-US patent
office or an International Search Report from an International Searching
Authority for a patent application filed via the Patent Cooperation Treaty or
document (s) cited in the application or the priority application.

This paper is submitted in accordance with:

[x] 6.   37 CFR 1.97(b): [within three months of filing or prior to first Office Action]
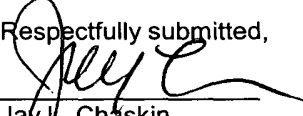
CERTIFICATE OF MAILING

I hereby certify that this correspondence is being deposited with the United States Postal Service
as First Class Mail in an envelope addressed to: Assistant Commissioner for Patents,
Washington, DC 20231, on the date indicated below.
By _Dolores K. Tillson_   Date: November $\mathcal{9}$, 2001
Dolores Tillson

[ ] 7.   37 CFR 1.97(c): [before Final Office Action or Allowance, whichever is earlier]; and

[ ] 8.   The required Certification made in item 11 below; or

[ ] 9.   The $240.00 fee specified in 37 CFR 1.17(p) for submission of this Information Disclosure Statement is authorized in item 14 below.

[ ] 10. 37 CFR 1.97(d): [before issue fee payment]; and

    a)   This is a petition for consideration of the subject Information Disclosure Statement. The petition fee of $130.00 required by 37 CFR 1.17(i)(1) is authorized in item 14 below. (Direct this letter to: "Attention PETITIONS EXAMINER" and if applicable include batch locator information, e.g., "Allowed Files, Batch _____, Date of Allowance_____") and

    b)   The required Certification is stated in item 11 below.

[ ] 11. Certification

    [ ] 12.   Each item or information contained in this Statement was first cited in a Search Report or communication from a non-US patent office or an International Search Report from an International Searching Authority for a patent application filed via the Patent Cooperation Treaty in a counterpart foreign patent application not more than three months prior to the filing of this Statement; or

    [ ] 13.   No item contained in this Statement was cited in a Search Report or communication from a non-US patent office or an International Search Report from an International Searching Authority for a patent application filed via the Patent Cooperation Treaty in a counterpart foreign patent application or, to the knowledge of the person signing this document after making reasonable inquiry, was known to any individual designated in 37 CFR 1.56(c) more than three (3) months prior to the filing date of this Statement.

[ ] 14. Payment of all applicable fees:

    ☐   Please charge all applicable fees associated with the submittal of this Information Disclosure Statement to Deposit Account No. 09-0470. An original and two (2) copies of this document are enclosed.

    ☐   Enclosed is a check in the amount of $_____in payment of all applicable fees associated with the submittal of this Information Disclosure Statement. An original and two (2) copies of this document are enclosed.

Respectfully submitted,

Jay L. Chaskin
Reg. No. 24030

Address: General Electric Company
3135 Easton Turnpike, Fairfield, CT 06431-0001
Fax: 203-373-3991
Tel: 203-373-2867

Form PTO-1449 (REV. 8-88)	U.S. DEPARTMENT OF COMMERCE PATENT AND TRADEMARK OFFICE	ATTY. DOCKET NO. 14XZ 00088	SERIAL NO.
INFORMATION DISCLOSURE CITATION (Use several sheets if necessary)		APPLICANT SUREDA ET AL.	
		FILING DATE	GROUP

U.S. PATENT DOCUMENTS

EXAMINER INITIAL		DOCUMENT NUMBER	DATE	NAME	CLASS	SUBCLASS	FILING DATE IF APPROPRIATE

J1050 U.S. PTO
10/011011
11/09/01

FOREIGN PATENT DOCUMENTS

		DOCUMENT NUMBER	DATE	COUNTRY	CLASS	SUBCLASS	TRANSLATION YES	NO

OTHER DOCUMENTS (Including Author, Title, Date, Pertinent Pages, Etc.)

		BALAKRISHNA HARIDAS ET AL. "PREDICTIVE ANALYSIS AT THE FOREFRONT OF MEDICAL PRODUCT DEVELOPMENT," MEDICAL DEVICE & DIAGNOSTIC INDUSTRY MAGAZINE, OCTOBER 1999, PP 1-10
		"SIMULATION OF THE IN VIVO DEVELOPMENT OF A PALMAZ-SCHATZ TYPE STENT IN A PARTIALLY OCCLUDED ARTERY", SUPERCOMPUTING INSTITUTE, RESEARCH BULLETIN ONLINE, VOL 14, NO. 3 JULY 1998
		HOLZAPFEL ET AL, "LARGE STRAIN ANALYSIS OF SOFT BIOLOGICAL MEMBRANES: FORMULATION AND FINITE ELEMENT ANALYSIS", COMPUTER METHODS IN APPLIED MECHANICS AND ENGINEERING, VOL 132, NO 1/02, MAY 15 1996 PAGES 45-61

EXAMINER		DATE CONSIDERED	

*EXAMINER: Initial if citation considered, whether or not citation is in conformance with MPEP 609. Draw line through citation if not in conformance and not considered. Include copy of this form with next communication to applicant.

Form PTO-1449 (REV. 8-88)	U.S. DEPARTMENT OF COMMERCE PATENT AND TRADEMARK OFFICE	ATTY. DOCKET NO. IAX200088	LEGAL NO.
INFORMATION DISCLOSURE CITATION		APPLICANT SUREDA ET AL.	
(Use several sheets if necessary)		FILING DATE	GROUP

U.S. PATENT DOCUMENTS

EXAMINER INITIAL		DOCUMENT NUMBER	DATE	NAME	CLASS	SUBCLASS	FILING DATE IF APPROPRIATE

FOREIGN PATENT DOCUMENTS

		DOCUMENT NUMBER	DATE	COUNTRY	CLASS	SUBCLASS	TRANSLATION YES	NO

OTHER DOCUMENTS

FINET, "ECHOGRAPHIE · ENDOCORONAIRE ET ANGIOPLASTE" ARCHIVES DES MALADIES DU COEUR ET DES VAISSEAUX") VOL. 92 NO. 11, NOVEMBER 1999 PAGES 1681-1689

EXAMINER		DATE CONSIDERED	

*EXAMINER. Initial if citation considered, whether or not citation is in conformance with MPEP 609. Draw line through citation if not in conformance and not considered. Include copy of this form with your communication to applicant.

INPI

**INSTITUT
NATIONAL DE
LA PROPRIETE
INDUSTRIELLE**

CASALONGA

17 . . .

GK 6/3

16/M

BUREAU CASALONGA ET JOSSE

8 AVENUE PERCIER
75008 PARIS

DEMANDE DE : BREVET
NO : 0015691000 DU 04/12/00
V/REF. : B99/2540FR AK/G

PARIS, LE 16 AOUT 2001

OBJET : NOTIFICATION D'UN RAPPORT DE RECHERCHE PRELIMINAIRE
AVEC REPONSE OBLIGATOIRE

Messieurs,

J'ai l'honneur de vous adresser, en annexe, le rapport de recherche préliminaire établi conformément à l'article R.612-57 du code de la propriété intellectuelle, citant les documents qui peuvent être pris en considération pour apprécier la nouveauté et l'activité inventive de l'invention, objet de votre demande.

Selon l'article R.612-59 du code précité, vous disposez d'un délai de **3 mois** à compter de la date de réception de ce rapport de recherche préliminaire pour y répondre par écrit. Avant l'expiration de ce délai, celui-ci peut être renouvelé une fois sur votre requête.

Suivant la catégorie des documents cités, vous pouvez être tenu à une obligation de réponse (par exemple, si le rapport de recherche préliminaire mentionne des documents de catégorie **X ou Y**). Dans ce cas, un papillon **rouge** est apposé sur cette lettre et le défaut de réponse entraînera le rejet de la demande. Dans le cas contraire, ce papillon est **jaune**.

Dans tous les cas, il est de votre intérêt en élaborant votre réponse, de tenir compte de tous les documents cités.
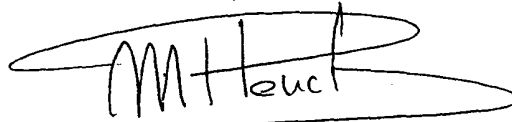
Selon les articles R.612-58 et R.612-60 du code précité, votre réponse peut consister :

- soit en de nouvelles revendications (en 3 exemplaires). Dans ce cas, vous devez signaler les changements apportés aux revendications initiales. Vous pouvez y joindre des observations qui mettent en évidence les caractéristiques techniques de ces nouvelles revendications qui échappent à l'opposabilité des antériorités citées.

- soit seulement en des observations qui ont alors pour objet de discuter l'opposabilité des antériorités citées.

Veuillez agréer l'expression de ma considération distinguée.

Pour le Directeur général de l'Institut national
de la propriété industrielle

Le Chef du département des brevets

Martine PLANCHE

Catégorie	DOCUMENTS CONSIDÉRÉS COMME PERTINENTS Citation du document avec indication, en cas de besoin, des parties pertinentes	Revendication(s) concernée(s)	Classement attribué à l'invention par l'INPI
Y	BALAKRISHNA HARIDAS, CLINTON A. HAYNES: "Predictive Analysis at the Forefront of Medical Product Development" MEDICAL DEVICE & DIAGNOSTIC INDUSTRY MAGAZINE, 'en ligne! octobre 1999 (1999-10), XP002173874 Extrait de l'Internet: <URL:http://devicelink.com/mddi/archive/99/10/009.html> 'extrait le 2001-07-30! * le document en entier *	1-7,9-11	A61B6/00 A61B19/00 G06F17/00 G06T17/00 G06T17/20
Y	"Simulation of the In Vivo Deployment of a Palmaz-Schatz Type Stent in a Partially Occluded Artery" SUPERCOMPUTING INSTITUTE, RESEARCH BULLETIN ONLINE, 'en ligne! vol. 14, no. 3, juillet 1998 (1998-07), XP002173875 Extrait de l'Internet: <URL:http://web.msi.umn.edu/general/Bulletin/Vol.14-No.3/july98.html> 'extrait le 2001-07-30! * le document en entier *	1-7,9-11	
A	HOLZAPFEL G A ET AL: "LARGE STRAIN ANALYSIS OF SOFT BIOLOGICAL MEMBRANES: FORMULATION AND FINITE ELEMENT ANALYSIS" COMPUTER METHODS IN APPLIED MECHANICS AND ENGINEERING,NORTH-HOLLAND, AMSTERDAM,NL, vol. 132, no. 1/02, '15 mai 1996 (1996-05-15), pages 45-61, XP000972573 ISSN: 0045-7825 * page 56 - page 59 *	1,11	

DOMAINES TECHNIQUES
RECHERCHÉS   (Int.CL.7)

G09B

-/--

1

Date d'achèvement de la recherche	Examinateur
3 août 2001	Szarowski, A

INPI
INSTITUT
NATIONAL DE
LA PROPRIETE
INDUSTRIELLE

**RAPPORT DE RECHERCHE
PRÉLIMINAIRE**

établi sur la base des dernières revendications
déposées avant le commencement de la recherche

N° d'enregistrement
national

FA 597502
FR 0015691

	DOCUMENTS CONSIDÉRÉS COMME PERTINENTS	Revendication(s) concernée(s)	Classement attribué à l'invention par l'INPI
Catégorie	Citation du document avec indication, en cas de besoin, des parties pertinentes		
D,A	G. FINET: "Échographie endocoronaire et angioplastie" ARCHIVES DES MALADIES DU COEUR ET DES VAISSEAUX, vol. 92, no. 11, novembre 1999 (1999-11), pages 1681-1689, XP001014246 * le document en entier *	1,11	
			DOMAINES TECHNIQUES RECHERCHÉS (Int.CL.7)

1

Date d'achèvement de la recherche	Examinateur
3 août 2001	Szarowski, A

CATÉGORIE DES DOCUMENTS CITÉS

X : particulièrement pertinent à lui seul
Y : particulièrement pertinent en combinaison avec un autre document de la même catégorie
A : arrière-plan technologique
O : divulgation non-écrite
P : document intercalaire

T : théorie ou principe à la base de l'invention
E : document de brevet bénéficiant d'une date antérieure à la date de dépôt et qui n'a été publié qu'à cette date de dépôt ou qu'à une date postérieure.
D : cité dans la demande
L : cité pour d'autres raisons

& : membre de la même famille, document correspondant

EPO FORM 1503 12.99 (P04C14)

industry   ■   ■   ▨   ⸱   ✉ email   🖨 print

An *MD&DI* October 1999 Column

P.D. OCT 1999
P. 1-10   10

DESIGN

Predictive Analysis at the Forefront of Medical Product Development

Predictive analysis and simulation of medical device and implant performance using nonlinear finite element analysis can significantly accelerate product development cycles while helping manufacturers to avoid costly mistakes.

Balakrishna Haridas and Clinton A. Haynes

The biomedical device and implant industry provides a unique and challenging environment for medical product development. Engineers are actively involved in the design, development, and manufacture of materials and devices intended for a variety of life-sustaining applications. Because the functions of such devices and implants can have varying levels of impact on the well-being of patients, FDA has three levels of classification for regulatory purposes—Class I, Class II, and Class III. The increasing levels of regulation from Classes I through III represent, in effect, a rigorous quality control program to ensure that new devices undergo adequate and, if required, extensive testing and trials to establish their performance prior to formal release into the U.S. market.

Understandably, the development cycle for a medical product can be quite complex, especially for Class II and Class III devices. The conventional product develop-ment process of design-build-test-rebuild typically involves several trial-and-error-based iterations of a concept prior to full-scale production. These iterations are costly and tax resources, especially since rework loops in the initial development phases of the device do not directly verify its in vivo function. Popular rapid prototyping technologies such as stereo-lithography, fused deposition modeling, and selective laser sintering allow design teams to duplicate part geometry and qualitatively verify design intent. Unfortunately, rapid prototyping does not provide any quantitative feedback on the functional mechanical performance of an actual device in vivo.

In the early stages of the development of a new device or implant, it is not desirable economically to manufacture functional prototypes of several concepts for in vivo testing. When prototypes are fabricated, the inability of a device design to deliver the intended function is established only after the organization has gone through an entire product development cycle. In this case, a change in the design could have a dramatic financial impact on the company that is developing the product.

Current approaches to medical device development can be significantly enhanced using such advanced computational methods as nonlinear finite element analysis (FEA). This computer-based simulation technology has experienced tremendous growth over the past 10 years. As a result, there are several commercial software programs available to the engineer appropriately trained in the theory and practical application of this analysis method.

The theoretical simulation techniques described below have a definite role in the engineering development cycle for medical devices or implants. While challenges do exist in the application of the technology, an engineer with the appropriate level of experience and training can effectively apply these methods to accelerate the product development process.

Predictive analysis will never completely replace prototyping and testing. However, drawing from past experience with this technology, in most cases predictive analysis tools limit the number of functional prototypes and trial testing, including expensive animal trials.[1,2] Effective integration of engineering-mechanics-based design decisions into the medical device development process is also usually achieved.

THE ROLE OF PREDICTIVE ANALYSIS AND SIMULATION

Two popular yet diametrically opposed perspectives on the intended role of predictive simulation in the medical products industry are both based on misconceptions. The first school of thought has reservations regarding the application of computer-based simulation. The reasoning behind this is that inputs to a computational simulation of the mechanics of a device and surrounding tissue sometimes appear to misrepresent the true boundary conditions or

material properties. The net result of this misconception is that engineering analysis and simulation as a tool is abandoned, and a trial-and-error process is adopted as the preferred product development strategy. The second school of thought believes that simulation will completely replace the need for all prototyping. While this has occurred to a limited extent in conventional engineering applications such as the automotive industry, it is not likely to occur within the medical device industry because of the kind of products involved.

The true role of computational simulation and predictive analysis lies between these two extremes. A carefully defined computational mechanics model of a device-tissue interaction problem can be invaluable to a biomedical designer in providing feedback on the relative merits and demerits of different design options, for example. In this sense, simulation of the mechanical performance of a medical device or implant in vivo using nonlinear FEA can be employed routinely at different phases of the product development cycle as deemed appropriate by a project team.

Most medical products involve materials, such as polymers, and manufacturing techniques (e.g., injection molding, extrusion, blow molding, thermoforming, and compression molding) that introduce significant variability in component performance. Designs must also account for biological variability in cases where the device interfaces directly with tissue. In this situation, highly variable tissue material properties play a significant role. Mechanical properties of living tissue are functions of several factors such as age, pathological state, type of tissue, and collagen-elastin-muscle content. The resulting device-tissue interaction problems involve severe nonlinearities in mechanical and material behavior. This is the underlying feature of most design problems involving polymeric components that interact with tissue, which is a highly nonlinear material. As a result, some form of in vitro or in vivo testing in animal models with a fully functional prototype is always required. Nonlinear FEA can be used as a complementary tool in conjunction with appropriate material descriptions to predict such nonlinear phenomena. This adds tremendous value to the product development process and dramatically reduces the risks associated with mechanical component design.

APPLICATIONS OF PREDICTIVE ANALYSIS AND SIMULATION

The growth and development of the application of nonlinear FEA technology as a predictive analysis tool has enabled its application in several areas of medical device design and manufacturing.[3] The diverse range of applications include such hard tissue implants and devices as:

- Fracture wires.
- Fixation pins (internal/external).
- Bone plates and screws.
- Total joint replacements.
- Dental implants.

Soft tissue implants and devices include:

- Vascular grafts.
- Percutaneous devices.
- Heart assist devices (pacemakers and LVADs).
- Ear and eye implants.
- Surgical tools.

As mentioned above, the role for predictive analysis tools can encompass several product development functions, such as upstream design concept evaluation, "what-if" material sensitivity studies, understanding tolerance effects, manufacturing and materials processing simulation, failure analysis in metallic and polymeric components, and generation of analytical data in support of 510(k) and premarket approval applications.

Applications of predictive analysis for the first three product design and development activities from the above list are described below. A forthcoming article will address the application of this technology to the design and optimization of manufacturing processes, as well as to problems in failure analysis in metallic and polymeric components in medical devices.

UPSTREAM DESIGN CONCEPT EVALUATION

One of the most effective applications of predictive simulation is upstream design concept evaluation in the earliest stage of the product development cycle, i.e., when a designer is conceptualizing the configuration of the device. Application of predictive nonlinear FEA at this stage facilitates physics-based quantitative ranking of several design concepts. The following case study is a good example of the application of FEA to these areas.
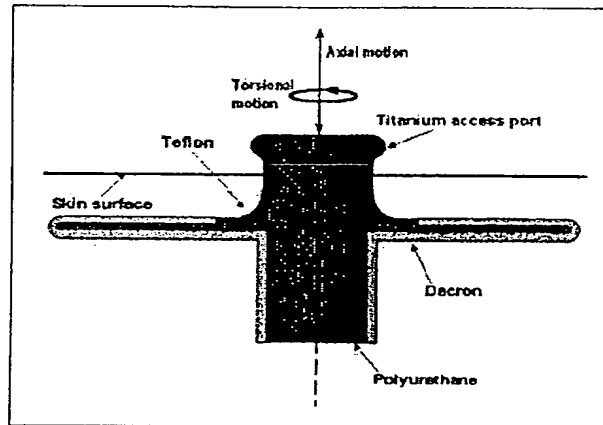
Figure 1. Schematic of a typical percutaneous device. Axial and torsional motions could develop stresses in the device as well as at the tissue-implant interface.

Case Study: Percutaneous Implant Evaluation. An example of the application of predictive analysis is the design evaluation of a conceptual percutaneous implant (Figure 1).[3]

Percutaneous implants are surgically introduced under the skin for long-term use.[4] These implants serve as conduits for the transfer of information in applications that can include drug delivery, blood monitoring, colorectal surgical procedures, pacemakers, and ports for kidney dialysis. Mechanical design issues for such devices include:

- Material selection.
- Minimization of tissue-device interface stresses.
- Optimization of implant geometry for various possible motions of the device.
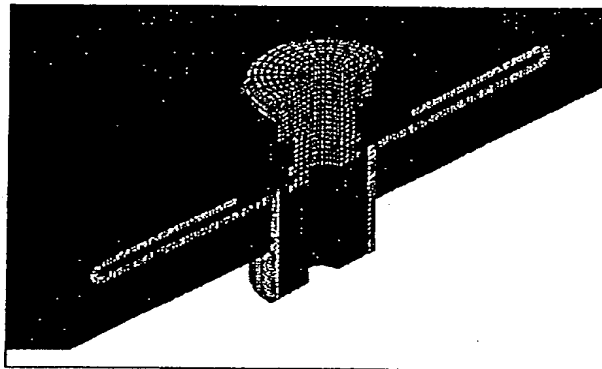
Figure 2. Finite element model of the percutaneous device, shown in Figure 1, implanted in skin.
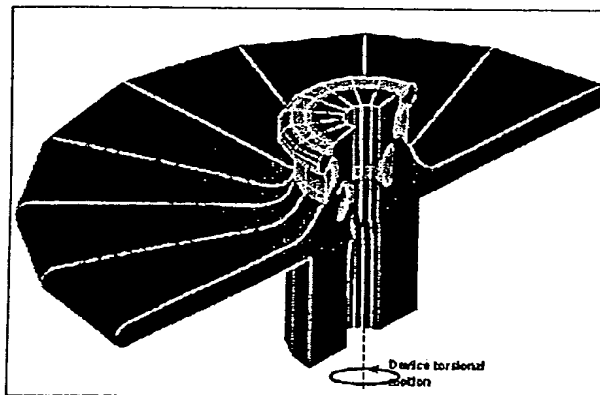
Figure 3. Von Mises stress in the device during torsional loading and motion.

A key issue in designing these implants relates to the local stiffness of the implant at the implant-tissue interface. A large mismatch in stiffness between the implant surface and the tissue will result in stress concentrations that could be detrimental to the implant material, the tissue, or both. Given that the properties of soft or hard tissue are very sensitive to changes in mechanical stimulus in vivo, a phenomenon known as Wolff's Law,[5] the engineering of the tissue-implant interface is extremely important. A predictive simulation model allows the performance of the design to be bounded in this sense. Nonlinear FEA results for the percutaneous implant example are shown in Figures 2 through 5. These simulations capture interlaminar stresses within the implant materials in addition to obtaining estimates of the loads transferred to skin across the Dacron-tissue interface.
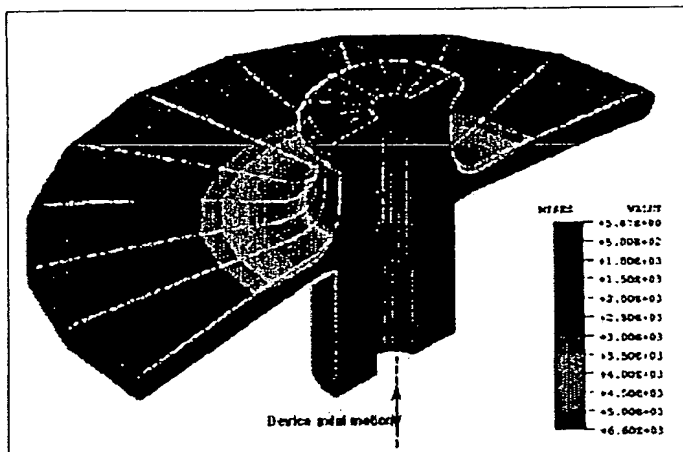
Figure 4. Von Mises stress in the device during axial loading and motion.
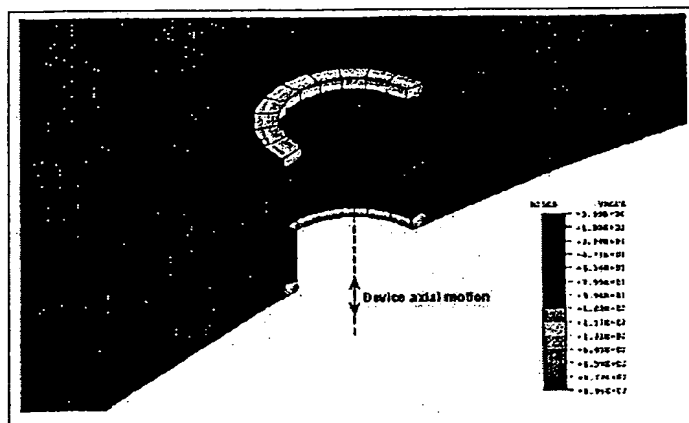
Figure 5. Stress in the skin layers during axial motion of the device.

Results from the nonlinear FEA simulation model of this percutaneous device can be used to drive changes in the design, which could include material selection or geometric changes that would ensure the long-term reliability of the device and minimize the mechanical stresses at the tissue-device interface. The efficiency of the seal at the port can also be evaluated with FEA and contact-stress analysis to determine the magnitude of the seal pressure. Because the seal is microbial, it is critical that a minimum contact pressure is maintained over time and across the range of manufacturing tolerances in the access port. Recently described methods of using FEA to analyze sealing and closure systems can be applied to this class of design problems.[6]

"WHAT-IF" MATERIAL SENSITIVITY STUDIES

The unique feature of designing a medical device for a load-bearing application is the fact that the device material chosen not only has to be biocompatible and FDA approved, but also must deliver the appropriate mechanical function within the design envelope. A computational model can be used to perform "what-if" evaluations to determine the optimal range of mechanical properties of the device material. This simulation can be leveraged to assess the effect of biological variability and resulting mechanical property differences in the tissue that could impact device performance. The measurement of the tissue mechanical properties, which are often highly nonlinear, can be characterized using specialized in vitro tests on cadaveric tissue, in vivo tests in animal tissue, or a combination of both.[7] Sample sizes for these tests can be controlled via statistical power analyses to deliver ±2σ, ±3σ, or even ±6σ range of properties (σ—standard deviation).[8] Such material data allow the simulation of the device-tissue interaction problem to be exercised over the entire range of statistical variability, allowing the function of the device and the materials to be fully assessed.

Case Study: Balloon Angioplasty Catheter Evaluation. Percutaneous transluminal angioplasty (PTA) is a surgical procedure performed to alleviate stenosed arteries by compressing the calcified plaque that can block the flow of blood.[9] The goals of this procedure are to enlarge the lumen of the stenosed vessel, to maintain the lumen over time, and to provide an intimal surface that promotes neo-intimal hyperplasia.
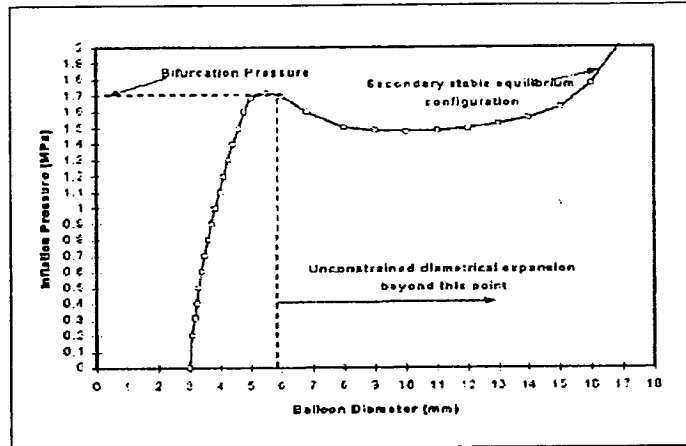
Figure 6. Pressure vs. diameter relationship for a typical balloon catheter during free inflation conditions.

A critical design variable that affects the performance of a balloon catheter in terms of geometry and material selection is its bifurcation pressure and subsequent inflation. The bifurcation pressure for an inflating membrane is the internal pressure required to initiate dilation, beyond which the growth of the membrane proceeds in an uncontrolled fashion (Figure 6). The mechanics of membrane inflation fall under a particular class of highly nonlinear phenomena called snap-through-bifurcation problems. Typical pressure vs. radius curves, illustrated in Figure 6 for balloon catheters, can be computed with a finite element model of free inflation (Figure 7) that incorporates the appropriate nonlinear material data for the polymer or elastomer used in the catheter. In general, these catheter materials can be described by hyperelastic or plasticity material models that are available in most leading nonlinear finite element codes.[1] The characterization of these materials, especially hyperelastic materials, has to be done carefully because a standard uniaxial tension test alone will not yield adequate data for balloon inflation simulations. Additional tests to characterize the response of the polymer under constrained conditions, such as biaxial stretching, must be performed to generate the appropriate material constants for input into the finite element calculations.

Prior knowledge of the bifurcation pressure is extremely useful to the designer of an angioplasty balloon system because the inflation of the membrane progresses in an unstable fashion beyond the bifurcation point. This can be seen in the form of large radial expansions with no increase in cavity pressure (Figure 6). The PTA balloon manufacturer would thus have useful information available regarding the window of operation of a given catheter and balloon design. Design variables, including material properties, wall thickness distribution, and geometry, could be used to control the initiation of the bifurcation and subsequent inflation characteristics of a given device.
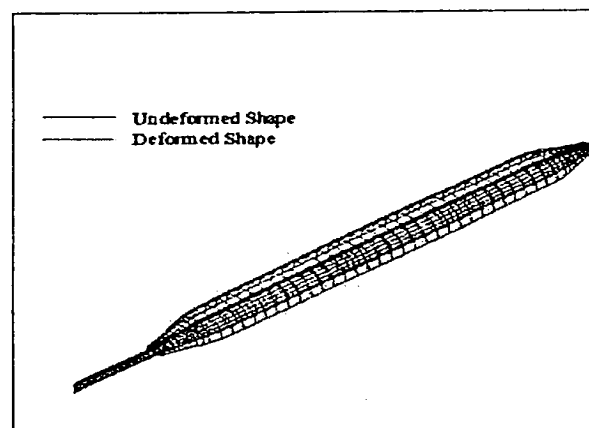
Figure 7. FEA simulation of free inflation of balloon catheter to determine bifurcation pressure.
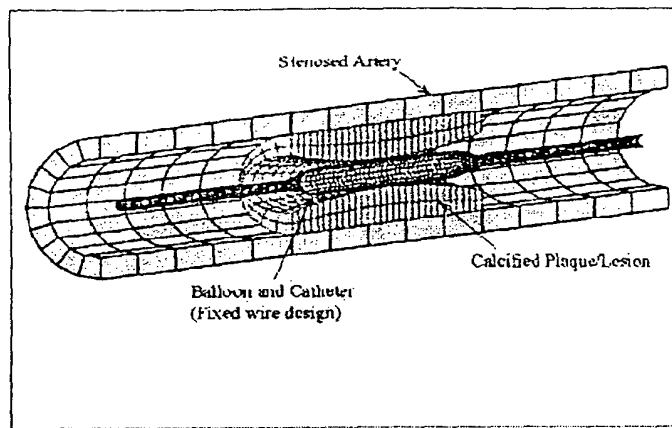
Figure 8. 3-D finite element model of stenosed artery with fixed wire balloon catheter prior to inflation.

Once the bifurcation pressure has been determined, the optimal balloon geometry and wall thickness can be determined by performing simulations of the surgical procedure. This requires finite element modeling of the balloon positioned within the lumen of the stenosis and then inflated against a virtual blocked vessel (Figures 8–10). This analysis requires characterization of the 3-D geometry of a stenosis/lesion using imaging and x-ray data, plaque material properties ranging from highly calcified to minimal calcification levels, and hyperelastic material properties for a normal artery through appropriate material testing.

As a starting point, this information is typically obtained from published data and research articles and is usually sufficient for design evaluation purposes. Such a virtual predictive simulation model is an ideal platform to generate catheter performance data in terms of the ability of the design to compress plaque without initiating tears at the plaque-intima interface. Intimal splitting of plaque is clinically detrimental to the success of the angioplasty procedure.[9] Evaluation of the catheter in this virtual model can also be exercised over a ±6σ range of plaque and artery properties as described earlier. The introduction of a supporting metal stent can also be simulated in the same model. In this case, the goal is to design in the stent the appropriate radial stiffness that would be required to support the dilated arterial cross section.

UNDERSTANDING TOLERANCE EFFECTS

Manufacturing tolerances have a significant impact on the performance of the many medical devices and implants that use polymeric materials. If the range of dimensional tolerances that are typical for the process is known, a predictive analysis model of the device can be assessed at the nominal as well as at the extremes of the expected dimensional variability. Analytical data generated from such models can be used in Monte Carlo simulations to generate the statistical range of the performance displayed by the device or implant.

Case Study: Evaluation of a Blood Vessel Ligation Clip System. Ligation clips are being used increasingly during surgical procedures as a means to temporarily ligate blood vessels that feed into the surgery site. These clips are usually loaded in cartridges and are dispensed into position by an actuating mechanism that drives a stack of clips in the cartridge through a rigid metallic channel (Figure 11). As the device is fired, the clips pass through a small bump-like feature in the channel called a retention bead. The force exerted by the surgeon to move the clips through the device is a direct function of the interference between the clip dimension (D) and the retention bead dimension (d). Depending on how the clips and channel were manufactured, there will be tolerances associated with the resulting interference that must be overcome during device actuation. These tolerances directly affect the force input that must be exerted by the surgeon. For example, metal clips formed by a bending operation will have dimensional variations caused by the varying degrees of elastic spring-back following the forming operation. Injection-molded clips, on the other hand, will exhibit variability caused by postmolding shrinkage and mold-tooling-induced tolerances.
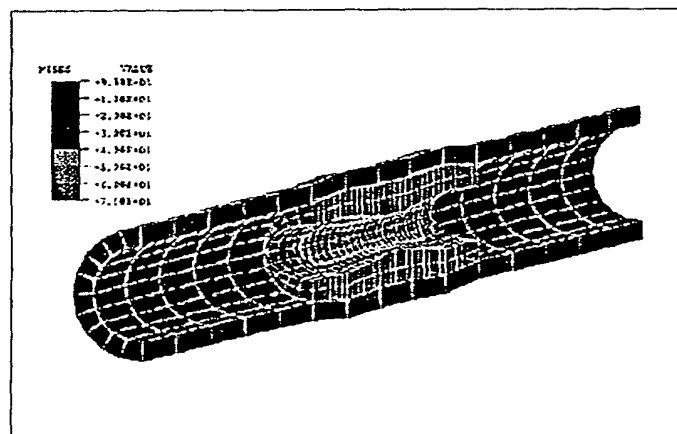
Figure 9. Plaque and artery deformations and effective stresses following balloon inflation.
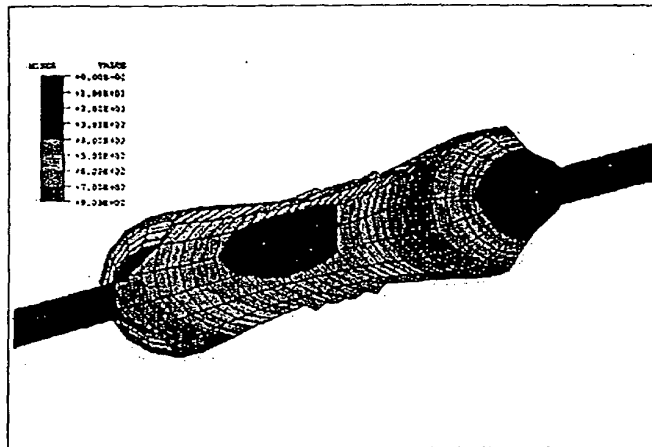

Figure 10. Balloon deformation and stresses following inflation.

A nonlinear FEA model of this device idealized as a three-clip system can be used to understand the effects of clip tolerances on the firing-force profile, as well as clip-to-clip interactions and stresses (Figure 12). The firing-force time curves described in Figure 13 are calculated by the simulations and describe the variability in the device firing force as a function of dimensional tolerance and of the stacking sequence of the clips (minimum-maximum-nominal in this case).

The unique aspect of this finite element model of the clip system is that there is a strong coupling between inertial and deformational effects in the clips. To fully capture this coupling, the model has been solved as a structural dynamics problem. A plot of the different energy quantities as a function of time, during firing of the three clips, clearly shows the energy accumulation from straining (i.e., deforming) each clip as it passes through the retention bead (Figure 14). It should be emphasized that almost all of this strain energy is converted into kinetic energy as each clip "jumps out" and moves downstream from the retention bead.

Another interesting result is that the force to fire the maximum-dimension clip is slightly lower than the value for the nominal-dimension clip (Figure 13). This is explained by the fact that the nominal clip slightly compresses the maximum clip because of clip-to-clip interaction during actuation. As a result, the effective dimension D is reduced to a value below the nominal at the point when the maximum clip passes through the retention bead, thus dropping the firing force of the clip to a value below the nominal.
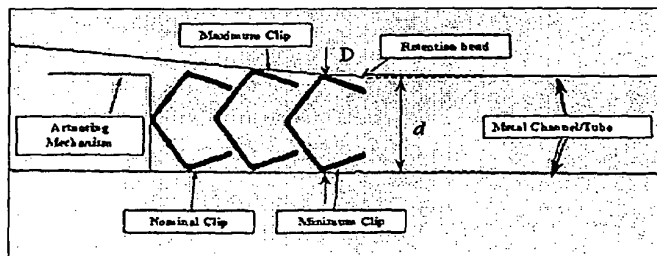
Figure 11. Conceptual layout of soft-tissue clips in a typical ligation device.
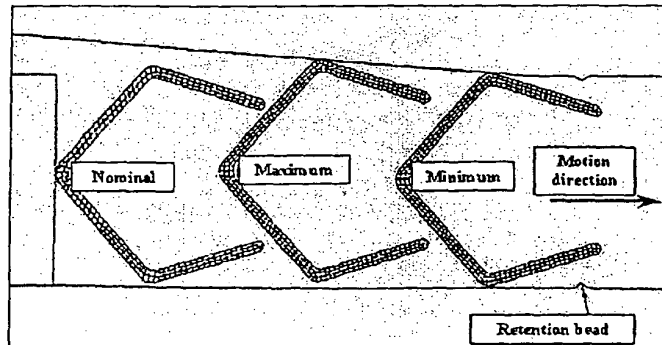
Figure 12. Finite element model of an idealized three-clip system.
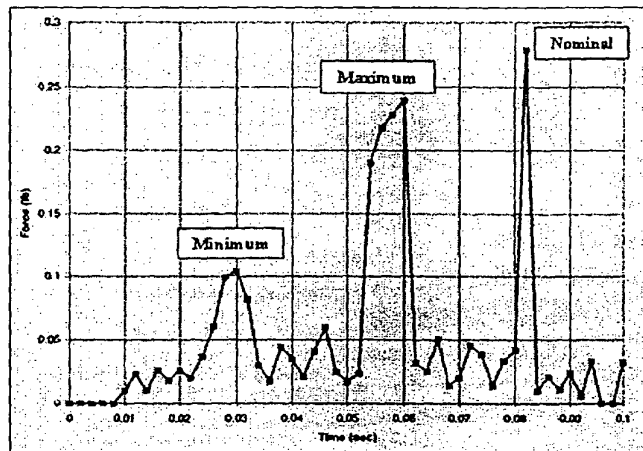
Figure 13. FEA solution for firing-force profile in the three-clip system.
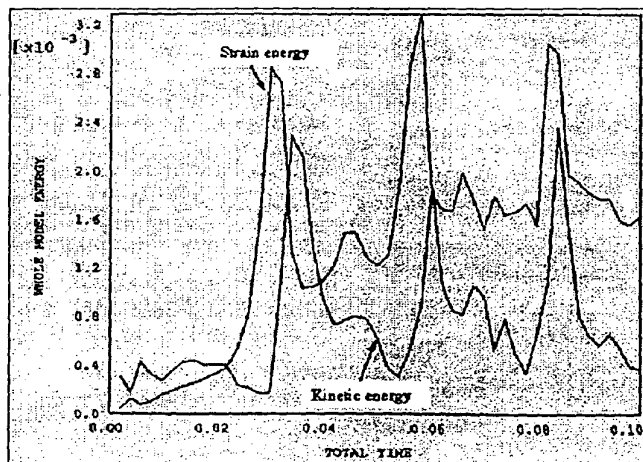
Figure 14. FEA solution for energy accumulation and release in the three-clip system.

Results from analyzing several stacking sequences of this three-clip system can be used to develop statistical models of clip firing to fully understand the effects of an arbitrary number of clips in the device. Once the clip is positioned around a blood vessel, an elastic-plastic finite element simulation can be used to calculate the force needed to achieve ligation in a blood vessel of given geometry and material properties (Figures 16 a–d). This solution can be used subsequently to either optimize the mechanical advantage of the firing mechanism, or to redesign the clip geometry to minimize the forming force and enhance the effectiveness of the ligation mechanism.

TECHNOLOGICAL CHALLENGES

Effective application of predictive analysis requires a clear understanding of the technological challenges associated with developing reasonable computational models of in vivo device function. The most significant issues routinely encountered include estimation of device loads and boundary conditions, proper representation of tissue geometry; proper representation of device and tissue material behavior, and quantitative validation of predictions with controlled small-scale tests.
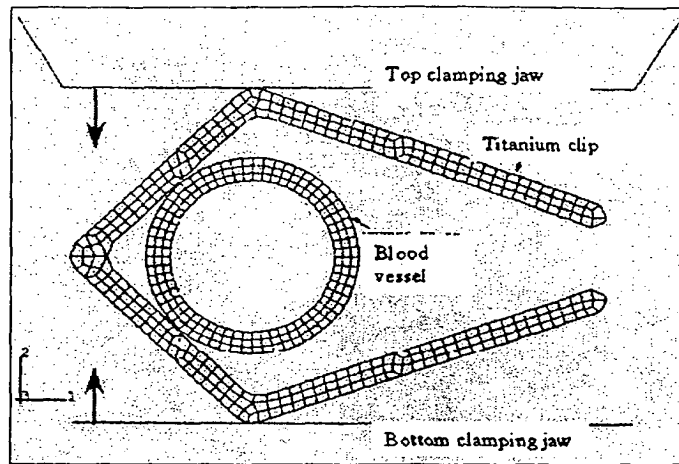
Figure 15. Finite element model for elastic plastic simulation of clip ligation and forming.
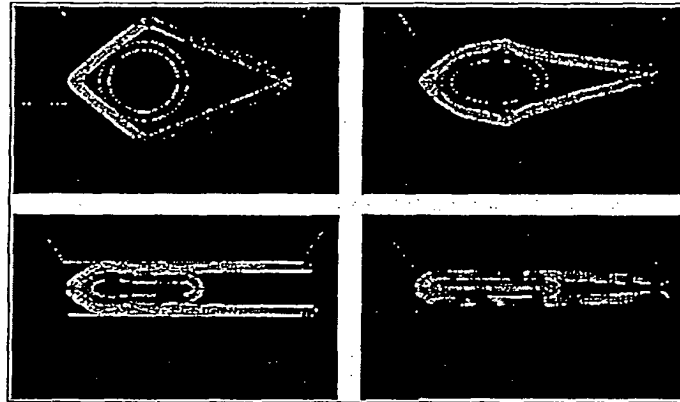
Figure 16 a–d. Evolution of shape and stresses in titanium clip during ligation.

Project teams considering the effective use of predictive analysis in the product development process should ensure that the above issues are adequately handled within the project timeline. Issues related to estimation of device loads and boundary conditions can be addressed by ensuring that an appropriate level of understanding has been achieved with regards to the design intent of the device. Biomechanical principles can be employed to derive realistic boundary conditions of the device or tissue for FEA model representation.[10] Tissue geometry and composition issues can be quantitatively addressed by appropriate imaging modalities, including computer-aided tomography, positron emission tomography, and x-ray, as well as microscopy techniques (e.g., histology, morphometry).[10,11] Device material response, in general, can be handled via conventional material-testing methods. If loads transmitted through tissue are important, however, characterization of tissue response will require fairly specialized testing in vivo or in vitro. Statistics play an important role in the analysis of tissue material data because of the need to understand variability of the properties at a desired level of significance.

CONCLUSION

Predictive analysis or simulation of medical devices and implants is a product development tool that can significantly accelerate the time to market and help manufacturers avoid costly mistakes early in the design process. The examples discussed above demonstrate the successful application of nonlinear FEA for evaluation of medical devices. They incorporate several of the technical challenges that are commonly faced in medical implant and device design. Although these technological challenges are inherent to the functional and regulatory requirements placed on medical products, they can be handled by carefully designed experiments and the application of biomechanical engineering principles.

Simulation methods offer the medical product designer an opportunity to explore the functional attributes of a design before tooling and trial-testing commitments are made. More importantly, the results of these simulations provide quantitative data and insights that are not available via prototyping methods alone. Issues such as manufacturing defect sensitivity, dimensional variability, material selection, and variability associated with user operation can be addressed to evaluate the robustness of a particular design concept.

With increasing demands being placed on medical device manufacturers by the market and by regulatory agencies, it is critical to establish a robust product development process that incorporates sound engineering. This can be achieved by incorporating a predictive engineering simulation-driven design evaluation process within the design loop. Drawing from past experience, such an integration of predictive simulation into the design cycle has always produced tangible benefits in terms of cost reduction, reduced time to market, and minimal rework loops.

REFERENCES

1. Haridas B and Butler DL, "Evaluation of a Class of Hyperelastic Constitutive Models for Finite Element Analysis of Experimentally Induced Defects in the Patellar Tendon" (paper presented at 18th Annual American Society of Biomechanics Meeting, Columbus, OH, October 1994).

2. DL Marriott , B Haridas, CA Haynes, "Modern Techniques of Design Analysis Applied to Polymeric Components" (paper presented at Pressure Vessels for Human Occupancy Conference, New Orleans, January 1999).

3. CA Haynes, CJ Matice, B Haridas, "Predictive Analysis, Simulation of High-Speed Vial Filling and Structural Analyses of Implants" (paper presented at OEMED, Chicago, 1997).

4. J Park, *Biomaterials Science and Engineering* (New York: Plenum Press, 1984).

5. J Wolff, "*Uber die innere architekture der knochen und ihre bedeutung fuer die frage vom knochenwachstum,*" *Archives in Pathology, Anatomy, and Physiology* 50.

6. CA Haynes, J Yuan, M DeYoung, "Design and Predictive Analysis of Plug, Claw, and Gasketed Closures" (paper presented at Society of Manufacturing Engineers Technical Program, Session on Closure Systems for Plastic Containers, Detroit, MI, 1998).

7. B Haridas et al., "Effects of Allograft Gamma Irradiation on the Cyclic Anterior/Posterior Response of the Reconstructed Knee" (paper presented at 40th Annual Meeting of the Orthopedic Research Society, New Orleans, 1994).

8. DC Montgomery, *Design and Analysis of Experiments* (New York: Wiley, 1991).

9. KL Gould, *Coronary Artery Stenosis*, (London: Elsevier, 1991).

10. B Haridas et al., "Transversely Isotropic Poroelastic Finite Element Simulations of the Intact and Surgically Translocated Flexor Tendon" (paper presented at ASME Bioengineering Division Summer Meeting, Big Sky, MT, 1999).

11. B Haridas et al., "In Vivo Stresses Correlate with Cellular Morphology in the Fibrocartilage-Rich Region of the Flexor Tendon" (paper presented at 44th Annual Meeting of the Orthopedic Research Society, New Orleans, March 16–19, 1998).

Balakrishna Haridas is a senior associate and technical leader in the Biomedical Simulation and Testing Group, Stress Engineering Services Inc. (Mason, OH), and Clinton Haynes is a senior principal and vice president of the firm.
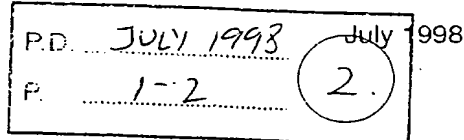
Back to the Table of Contents

Supercomputing Institute

Research Bulletin

Newsletter of the University of Minnesota Supercomputing Institute

P.D. JULY 1998
P. 1-2 2.

Simulation of the *In Vivo* Deployment of a Palmaz-Schatz Type Stent in a Partially Occluded Artery

B alloon angioplasty has proven to be an effective alternative to more invasive surgical procedures for the treatment of coronary disease, the leading cause of death in the United States. The goal of balloon angioplasty is to permanently increase the luminal size of a blood vessel that has been expanded by the inflation of a balloon at high pressure within the narrowed vessel segment to mechanically remove plaque deposition responsible for occlusion.

During angioplasty, a mechanical device known as a stent may be deployed at the site of vascular injury. Stents may be fabricated from a number of biocompatible materials, typically metals, and are preferably radio-opaque. Optimal stent deployment technique leads to uniform circumferential expansion and very close apposition to the vessel wall.

Unfortunately, balloons and stents are not designed for deployment as matching systems. Physicians often rely on personal preference and experience in selecting a combination of angioplasty balloons and stents. This may lead to inconsistent expansion of system components against the vascular wall. Stent deployment in an irregularly occluded or eccentric lumen can be particularly problematic.
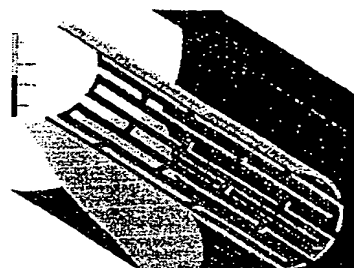
Undeployed stent eccentric arterial lumen

Professor William Gleason in the Department of Laboratory Medicine and Pathology at the University of Minnesota and Svenn Borgersen of BIOSIMulations Inc., Eagan, Minnesota used a Palmaz-Schatz type stent geometry as the basis for development of a three dimensional finite element analysis (FEA) model to simulate stent deployment within a partially occluded, asymmetric arterial lumen as shown in the figures. The purpose of the analysis was to examine the effects of an asymmetric lumen on deployed stent geometry and stress levels.

Model development and analysis were based on the mentat/marc k6.2 fea software from MARC Analysis Research Corporation, Palo Alto, California. The model consisted of eight noded, isoparametric, hexahedral elements. This element type has three translational degrees-of-freedom per node and a total of twenty-four degrees-of-freedom per element with eight Gaussian integration points. The model allows for large displacement, geometric stiffening, non-linear material properties, and full three dimensional contact. For this study, vascular walls and lumen occlusion surfaces were represented as three dimensional mathematically rigid boundaries. In order to evaluate anticipated stress concentration effects due to geometry at junctions of longitudinal and circumferential stent members, model mesh refinement was included at these locations.

Expansion of the stent to its maximum design configuration was accomplished using a uniformly distributed loading by use of a follower force on the internal surfaces of the stent. The magnitude of the pressure load was increased incrementally until the stent conformed to the simulated vascular geometry or the ultimate strength of the material was exceeded.

The obtained results clearly illustrated the inherent risks of deploying this type of stent in an asymmetric lumen: asymmetric deployed geometry, crippling of the structure, and non-conformity of the stent to the vascular lumen. A stent deployed under these conditions could be succeptible to collapse. Lack of structural stability and high stress level implied that sharply reduced mechanical fatigue design life may be anticipated.

These researchers have conducted a number of modeling studies of various stent types, geometries, and materials. These have included stent only, stent and catheter balloon only, and stent/catheter balloon/arterial wall. In general, good qualitative correlation has been achieved between the predicted deployed stent geometry obtained from the stent models and the observed deployed stent geometry obtained empirically.

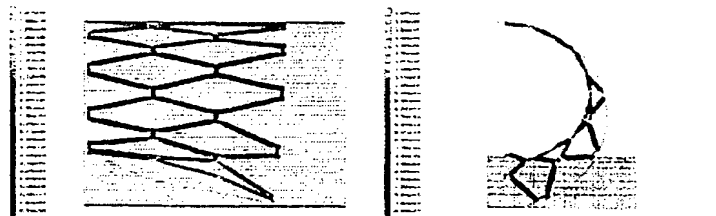Additional work is in progress to extend the computational results for other stent geometries, types, materials, stent coating materials, effects of stent/balloon combinations, and evaluation of deployment strategies.
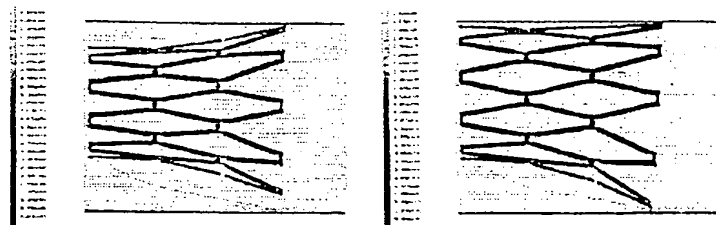
Eccentric arterial lumen with 50% stent deployment

Eccentric arterial lumen with 80% stent deployment

Side view of fully expanded stent design condition

End view of fully expanded stent design condition

This information is available in alternative formats upon request by individuals with disabilities. Please send email to alt-format@msi.umn.edu or call 612-625-1818.

XP-000972573

Large strain analysis of soft biological membranes: Formulation and finite element analysis

Gerhard A. Holzapfel[a,*], Robert Eberlein[b], Peter Wriggers[b], Hans W. Weizsäcker[c]

[a]*Division of Applied Mechanics, Department of Mechanical Engineering, Stanford University, Stanford, CA 94305-4040, USA*
[b]*Institut für Mechanik, TH Darmstadt, Hochschulstraße 1, D-63289 Darmstadt, Germany*
[c]*Physiologisches Institut, Karl Franzens Universität Graz, Harrachgasse 21, A-8018 Graz, Austria*

Abstract

This paper presents a general formulation of thin incompressible membranes and investigates the behavior of soft biotissues using the finite element method. In particular the underlying hyperelastic model is chosen to examine the highly non-linear constitutive relation of blood vessels which are considered to be perfectly elastic, homogeneous and (nearly) incompressible. First, the stress–deformation relation and the elastic tangent moduli are derived in a very general material setting which is subsequently specified for blood vessels in terms of Green–Lagrangian strains. Based on the principle of virtual work the finite element equations are provided and briefly discussed. Consistent linearization of the weak form of equilibrium and the external pressure term ensures a quadratic convergence rate of the iterative solution procedure. On the computational side of this work an effort was undertaken to show a novel approach on the investigation of soft tissue biomechanics. Representative numerical analyses of problems in vascular mechanics are discussed that show isochoric finite deformations (large rotations and large strains). In particular, a numerical simulation of the interaction between an inflated balloon catheter and a plaque deposit on the wall of a blood vessel is presented.

1. Introduction and overview

The objective of this study is to present a new numerical approach to the mechanical behavior of biotissues—in particular of blood vessels—which is based on the framework of non-linear continuum mechanics. One novel contribution to the field of computational mechanics is the Finite-Element (FE) simulation of the rat abdominal aorta and of the angioplasty, a technique in which an inflated balloon catheter interacts with a diseased blood vessel with the purpose to widen the lumen of the vessel. The numerical analyses have been managed on the basis of a hyperelastic biomaterial proposed by Fung and co-workers [1–3]. An implementation of the constitutive model within a finite element context has never been taken notice of in the literature, as far as the authors are aware.

Often the attempt is made to simulate soft vascular tissues with isotropic thin-walled (latex) rubber tubes (see e.g. [4–6]), which is a reasonable first approximation to the actual material behavior if the blood pressure domain of arteries is considered far below the physiological range. In fact within the range of low pressures the artery reacts at small strains, displays 'rubber-like' elastic behavior and may

---

* Corresponding author. Permanent address: Department of Mechanical Engineering, Technical University Graz, Kopernikusgasse 24/1, A-8010 Graz, Austria.

be modeled, e.g. by means of the classical isotropic neo-Hookean or Mooney–Rivlin potentials (see [7, 8]). However, a blood vessel under physiological conditions and higher internal pressures behaves as a mechanical *anisotrope* (cylindrical-orthotrope), primarily recognized by Patel and Frey [9], which to model and to analyze is our main goal. A rubber-based constitutive model is certainly *not* an adequate material for simulating arteries over wide ranges of deformations.

Vascular walls are (1) (nearly) incompressible for in vivo strains (first shown by Carew et al. [10]), (2) perfectly elastic (see e.g. [11]) and (3) show significant stiffening effects with increasing strains and internal pressures. In general, an artery is considered to be (4) homogeneous throughout the entire wall thickness and (5) free of residual stresses and strains, which in fact is disproved by the early work of Roach and Burton [12] (who indicate the significantly different mechanical behavior of elastin and collagen in the vascular wall), and by McDonald [13, p. 260] (who addresses an observation for the first time, namely, that an arterial strip which is cut through the thickness will open up), respectively.

Properties (1) and (2) are generally accepted in the literature, while the last two considerations are very open to question and still an area of ongoing research in physical modeling of biotissues, e.g. in recent studies the artery wall is regarded as a three-concentric-layered composite material (from the lumen outward: intima, media and adventitia) with different mechanical properties in the zero-stress state (see [14, 15]). For recent studies on residual stresses (see e.g. [15–17]), however, the biomechanical importance of residual stresses and strains was already recognized [18].

Based on assumptions (1)–(5) there are some phenomenological constitutive models in the literature with the same objective, namely, to correlate closely with experimental stress–deformation data for the entire occurring finite strain domain. The material models which are proposed in the form of more or less accurate strain (stored)-energy functions (potentials) are either given in a logarithmic form (see [19–21]), in a polynomial type (see [22–24]) or in the most commonly used exponential form presented in [14, 25–28] and in [1–3] which was also adopted in this paper. A selected review of the literature for constitutive laws of arterial walls was recently presented by Hayashi [21]. A review of a numerical approach in arterial wall mechanics with the FE method was given in a recent summary paper by Simon et al. [29].

The theoretical side of the paper starts with a review of the basic equations for thin incompressible membrane surfaces. The formulation encompasses large strain elasticity and is exclusively based on the right Cauchy–Green tensor and the principal stretches as a strain measure. Explicit expressions for the stresses and the symmetric tangent moduli are directly derived from the stored-energy function and are provided in a form which is independent of any particular choice of a hyperelastic material. Observe that for membranous structures it is sufficient to use only the tangential stresses in the deformed membrane surface (plane stress state). Within this two-dimensional approach the plane stress condition is imposed by introducing an additional constraint in the potential through an arbitrary scalar (Lagrangian multiplier) known as the hydrostatic pressure. The pressure which can always be expressed in closed form enforces the plane stress condition exactly. Next, we particularize the frame-invariant strain–energy function for analyzing the highly non-linear stress–strain response of an arterial wall. The consistent linearized tangent moduli is explicitly given as a novel result.

With regard to a numerical simulation which is based on the FE method, the principle of virtual work is introduced. A consistent linearization of the weak form of equilibrium leads to the governing basic equations essential for a FE simulation. For problems involving highly deformable elastic membranes, the pressure load is generally deformation dependent, which must be accounted for in the formulation. Special emphasis is devoted to the linearization of the external pressure term. A spatial discretization of a continuous membrane represented by assembling a finite number of displacement-based finite elements leads to the tangent stiffness relation and to the global residual force (out-of-balance force) which ensures quadratic convergence within Newton's method.

On the computational side of the paper, numerical results are illustrated for two selected axi-symmetrical problems of soft-tissue engineering undergoing finite strains: the hyperelastic model was fitted to experimental data obtained from a rat abdominal aorta. The contact of a balloon catheter on atheromatous plaque deposits located at the innermost layer of the wall of an artery is particularly addressed.

In this section we derive the basic equations used to describe the finite strain behavior of thin membrane surfaces which are assumed to be hyperelastic and incompressible. For a more comprehensive study on finite strain elasticity the reader may be referred to the standard books (e.g. [30–32]).

The presentation of a hyperelastic constitutive relationship which approximates the mechanical behavior of blood vessels closes the section.

2.1. Kinematics of deformation and strain–energy function

Consider a hyperelastic membrane (part of $\mathbb{R}^3$) undergoing large deformations (rotations and strains) which carry a material particle initially located at position $X = X(\Theta^\alpha)$ ($\Theta^\alpha|_{\alpha=1,2}$ are curvilinear Gaussian coordinates) into a spatial position $x = x(\Theta^\alpha)$ through the displacement vector $u := x - X$. Accordingly, we define a reference placement as $\mathscr{B}_0 \subset \mathbb{R}^3$ and a current placement (deformed configuration) as $\mathscr{B} \subset \mathbb{R}^3$.

The tangential vectors G_α and the external unit normal vector field N (by the cross product) are represented as

$$G_\alpha := \frac{\partial X}{\partial \Theta^\alpha} = X_{,\alpha} , \qquad N = \frac{G_1 \times G_2}{|G_1 \times G_2|} . \tag{1}$$

The Gaussian frame $G_A := \{G_\alpha, N\}$ forms a right-handed vector triad. Let G^A be the reciprocal basis, such that $\delta_\alpha^\beta = \langle G_\alpha, G^\beta \rangle$ and $G_{\alpha\beta} = \langle G_\alpha, G_\beta \rangle$, where δ_α^β denotes the Kronecker delta, $\langle \cdot, \cdot \rangle$ the Euclidean inner product and $G_{\alpha\beta}$ the metric coefficients, respectively. Similar definitions are introduced for the current configuration and are subsequently denoted by lower case letters.

The measure of deformation based on the two-dimensional theory is described by the symmetric right Cauchy–Green tensor C which is expressed by the material deformation gradient F. i.e.

$$C := F^T F = g_{\alpha\beta} G^\alpha \otimes G^\beta , \qquad F := \nabla x = g_\alpha \otimes G^\beta . \tag{2}$$

According to the representation theorems for invariants (see Section 10 in [30]), the strain–energy function $\mathscr{W}$ (per unit reference volume) for hyperelastic materials may be formulated as functions of the strain invariants (see [30, p. 317])

$$\mathscr{W} = \hat{\mathscr{W}}(I_A) = \hat{\mathscr{W}}(I_1, I_2, I_3) , \tag{3}$$

satisfying the condition $\hat{\mathscr{W}}(1,1,1) = 0$, where $\{I_A\}_{A=1,2,3}$ characterizes the three principal invariants of the right Cauchy–Green tensor $\hat{C} := \hat{C}_{AB} G^A \otimes G^B$, which are defined with respect to principal axes and a Cartesian basis as follows:

$$I_1 = \hat{I}_1(\hat{C}) := \text{tr}[\hat{C}] = \hat{C}_{11} + \hat{C}_{22} + \hat{C}_{33} ,$$

$$I_2 = \hat{I}_2(\hat{C}) := \frac{1}{2}\{(\text{tr}[\hat{C}])^2 - \text{tr}[\hat{C}^2]\} = \hat{C}_{11}\hat{C}_{22} + \hat{C}_{11}\hat{C}_{33} + \hat{C}_{22}\hat{C}_{33} . \tag{4}$$

$$I_3 = \hat{I}_3(\hat{C}) := \det[\hat{C}] = \hat{C}_{11}\hat{C}_{22}\hat{C}_{33} .$$

Equivalently, $\mathscr{W}$ can be formulated in the alternative form

$$\boxed{\mathscr{W} = \hat{\mathscr{W}}(\lambda_A) = \tilde{\mathscr{W}}(\lambda_1, \lambda_2, \lambda_3)} , \tag{5}$$

where $\{\lambda_A^2\}_{A=1,2,3}$ are the three real and positive (and non-zero) eigenvalues of the eigenvalue problem $(\hat{C} - \lambda_A^2 1)e_A = 0$ and correspond to the three eigenvectors $\{e_A\}_{A=1,2,3}$ (principal directions of strains). The three values $\{\lambda_A\}_{A=1,2,3}$ are called principal stretches and $1 = G_A \otimes G^A$ denotes the identity tensor.

The invariants of Eq. (4) expressed as functions of λ_A^2 are given as

$$I_1 = \lambda_1^2 + \lambda_2^2 + \lambda_3^2, \qquad I_2 = \lambda_1^2\lambda_2^2 + \lambda_1^2\lambda_3^2 + \lambda_2^2\lambda_3^2, \qquad I_3 = \lambda_1^2\lambda_2^2\lambda_3^2. \tag{6}$$

Incompressible materials have the property that the volume is preserved, which requires the following well-known condition (see e.g. [30, p. 71])

$$J = \frac{\mathrm{d}v}{\mathrm{d}V} = I_3^{1/2} = \det[\hat{C}]^{1/2} \equiv 1, \tag{7}$$

or rewritten in the form of principal stretches, with Eq. (6)$_3$,

$$\boxed{\lambda_1\lambda_2\lambda_3 = 1}, \tag{8}$$

where the dilatational ratio J characterizes the ratio between the incremental deformed volume $\mathrm{d}v$ of a body and its corresponding incremental undeformed volume $\mathrm{d}V$.

Through condition (8), the third principal stretch normal to the membrane degenerates to a dependent value, namely,

$$\lambda_3 = \frac{1}{\lambda_1\lambda_2}. \tag{9}$$

Therefore, the current thickness of the membrane h is always determined by relation $\lambda_3 = h/H$, where H denotes the initial thickness. Now, with help of Eq. (9), the non-vanishing components of the right Cauchy–Green strain tensor $\hat{C}$ in terms of principal stretches are given in the convenient matrix setting:

$$\hat{C}_{AB} = \begin{bmatrix} \hat{C}_{11} & 0 & 0 \\ 0 & \hat{C}_{22} & 0 \\ 0 & 0 & \hat{C}_{33} \end{bmatrix} = \begin{bmatrix} \lambda_1^2 & 0 & 0 \\ 0 & \lambda_2^2 & 0 \\ 0 & 0 & (\lambda_1\lambda_2)^{-2} = (h/H)^2 \end{bmatrix}. \tag{10}$$

2.2. General formulation of the stress and elasticity tensor for incompressible membranes

For *incompressible* hyperelastic continua the strain–energy density $\mathcal{W}^*$ is given through the addition of a Lagrangian multiplier $\bar{p}$, i.e.

$$\mathcal{W}^* = \mathcal{W} + \bar{p}(J - 1), \tag{11}$$

wherein $\mathcal{W}$ describes the *isochoric* deformation and $\bar{p}$ is an unknown scalar with the significance of a hydrostatic pressure, respectively.

The stress-deformation relation for a *Green elastic* or *hyperelastic* material is generated from the continuous strain–energy function $\mathcal{W}$, Eq. (11), by the relation

$$\hat{S} = \frac{\partial\mathcal{W}^*}{\partial\hat{E}} = 2\frac{\partial\mathcal{W}}{\partial\hat{C}} + 2\bar{p}\frac{\partial J}{\partial\hat{C}}, \tag{12}$$

where $\hat{E} := \frac{1}{2}(\hat{C} - 1)$ is the Green–Lagrangian (material) strain tensor and $\hat{S} := \hat{S}_{AB}G^A \otimes G^B$ denotes the corresponding work conjugate second Piola–Kirchhoff stress tensor. For a membrane, i.e. $E := E_{\alpha\beta}G^\alpha \otimes G^\beta$ with definition $2E_{\alpha\beta} := g_{\alpha\beta} - G_{\alpha\beta}$ (see e.g. [33]) and $S = \partial\mathcal{W}/\partial E := S_{\alpha\beta}G^\alpha \otimes G^\beta$, respectively. With the partial (Fréchet) derivative of quantity J relative to the symmetric strain tensor $\hat{C}$ (see [30, p. 25]), i.e.

$$2\frac{\partial J}{\partial\hat{C}} = J\hat{C}^{-1}, \tag{13}$$

and the incompressibility condition given by Eq. (7)$_4$, relation (12)$_2$ can be rewritten in the form (compare Fung [34, Eq. (12), p. 450])

$$\hat{S} = 2\frac{\partial \mathcal{W}}{\partial \hat{C}} + \bar{p}\hat{C}^{-1} \qquad \Leftrightarrow \qquad \hat{S}_{AB} = 2\frac{\partial \mathcal{W}}{\partial \hat{C}_{AB}} + \bar{p}\hat{C}^{-1}_{AB} \tag{14}$$

where $\hat{C}^{-1}$ characterizes the inverse right Cauchy–Green tensor.

With the use of the chain rule and Eqs. (9), (10), (14)$_2$ a straightforward computation shows the principal values of the symmetric Piola–Kirchhoff stresses, which are given in the following matrix setting:

$$\hat{S}_{AB} = \begin{bmatrix} \dfrac{1}{\lambda_1}\dfrac{\partial \mathcal{W}}{\partial \lambda_1} + \dfrac{\bar{p}}{\lambda_1^2} & 0 & 0 \\[2ex] 0 & \dfrac{1}{\lambda_2}\dfrac{\partial \mathcal{W}}{\partial \lambda_2} + \dfrac{\bar{p}}{\lambda_2^2} & 0 \\[2ex] 0 & 0 & \lambda_1\lambda_2\dfrac{\partial \mathcal{W}}{\partial \lambda_3(\lambda_1\lambda_2)} + \bar{p}\lambda_1^2\lambda_2^2 \end{bmatrix} . \tag{15}$$

Furthermore, using the plane stress constraint ($\hat{S}_{33} \overset{!}{=} 0$) the third row of Eq. (15) allows the hydrostatic pressure to be explicitly expressed as

$$\bar{p} = -\frac{1}{\lambda_1\lambda_2}\frac{\partial \mathcal{W}}{\partial \lambda_3(\lambda_1,\lambda_2)} . \tag{16}$$

Observe that for *membranous structures* the incompressibility condition is already incorporated due to Eq. (9) and the Lagrangian multiplier $\bar{p}$ introduced in Eq. (11) serves here as an arbitrary scalar function to enforce the plane stress condition.

Hence, a back-substitution of the pressure into relations (15)$_1$, (15)$_2$ leads to the following two non-zero components $S_\alpha|_{\alpha=1,2}$, i.e.

$$S_1 := \hat{S}_{11} = \frac{1}{\lambda_1}\frac{\partial \mathcal{W}}{\partial \lambda_1} - \frac{1}{\lambda_1^3\lambda_2}\frac{\partial \mathcal{W}}{\partial \lambda_3(\lambda_1,\lambda_2)} ,$$
$$S_2 := \hat{S}_{22} = \frac{1}{\lambda_2}\frac{\partial \mathcal{W}}{\partial \lambda_2} - \frac{1}{\lambda_1\lambda_2^3}\frac{\partial \mathcal{W}}{\partial \lambda_3(\lambda_1,\lambda_2)} . \tag{17}$$

Through a rotational transformation, the principal stresses S_α can be easily converted in stresses acting in any arbitrary position. Alternative stress measures are obtained by suitable transformations, e.g. the stress response in the Eulerian (spatial) description—the Cauchy–stress tensor σ for a membrane—follows with a push forward operation and the incompressibility condition (7)$_4$, i.e. $\sigma = FSF^T$, with F defined in (2)$_2$.

In the next part of this section the symmetric fourth-order tensor $\hat{\mathbb{C}}$—the elastic tangent moduli in the Lagrangian description—is derived by linearizing the second Piola–Kirchoff stress tensor. Differentiate Eq. (12)$_2$ once more with respect to $\hat{E}$ and use the chain rule, then we obtain an explicit expression for the desired consistent 'incompressible' moduli:

$$d\hat{S} = 2\underbrace{\frac{\partial \hat{S}}{\partial \hat{C}}}_{\hat{\mathbb{C}}} : \frac{1}{2}d\hat{C} \quad \text{with} \quad \boxed{\hat{\mathbb{C}} = 4\left[\frac{\partial^2 \mathcal{W}}{\partial \hat{C}^2} + \bar{p}\frac{\partial^2 J}{\partial \hat{C}^2} + \frac{\partial \bar{p}}{\partial \hat{C}} \otimes \frac{\partial J}{\partial \hat{C}}\right]} , \tag{18}$$

in components, i.e.

$$\mathbb{C}_{ABCD} = 2\frac{\partial \hat{S}_{AB}}{\partial \hat{C}_{CD}} = 4\left[\frac{\partial^2 \mathcal{H}}{\partial \hat{C}_{AB} \partial \hat{C}_{CD}} + \bar{p}\frac{\partial^2 J}{\partial \hat{C}_{AB} \partial \hat{C}_{CD}} + \frac{\partial \bar{p}}{\partial \hat{C}_{AB}}\frac{\partial J}{\partial \hat{C}_{CD}}\right] . \tag{19}$$

Analogous to the structure presented in Eq. (15), the components of the elastic moduli, i.e. (19), may be expressed in terms of principal stretches by means of Eqs. (9), (10), (13). Hence, with the plane stress condition, the elasticity tensor components for incompressible membrane shells are summarized in the following material matrix denoted by D, i.e.

$$D = \begin{bmatrix} \dfrac{1}{\lambda_1}\dfrac{\partial}{\partial \lambda_1}\left(\dfrac{1}{\lambda_1}\dfrac{\partial \mathcal{H}}{\partial \lambda_1}\right) - \dfrac{2\bar{p}}{\lambda_1^4} + \dfrac{1}{\lambda_1^3}\dfrac{\partial \bar{p}}{\partial \lambda_1} & \dfrac{1}{\lambda_2}\dfrac{\partial}{\partial \lambda_2}\left(\dfrac{1}{\lambda_1}\dfrac{\partial \mathcal{H}}{\partial \lambda_1}\right) + \dfrac{1}{\lambda_1^2 \lambda_2}\dfrac{\partial \bar{p}}{\partial \lambda_2} \\[4mm] \dfrac{1}{\lambda_2}\dfrac{\partial}{\partial \lambda_2}\left(\dfrac{1}{\lambda_1}\dfrac{\partial \mathcal{H}}{\partial \lambda_1}\right) + \dfrac{1}{\lambda_1^2 \lambda_2}\dfrac{\partial \bar{p}}{\partial \lambda_2} & \dfrac{1}{\lambda_2}\dfrac{\partial}{\partial \lambda_2}\left(\dfrac{1}{\lambda_2}\dfrac{\partial \mathcal{H}}{\partial \lambda_2}\right) - \dfrac{2\bar{p}}{\lambda_2^4} + \dfrac{1}{\lambda_2^3}\dfrac{\partial \bar{p}}{\partial \lambda_2} \end{bmatrix} . \tag{20}$$

Herein, $\bar{p}$ is the hydrostatic pressure expressed in Eq. (16) and its derivatives with respect to $\lambda_a|_{a=1,2}$ are computed as

$$\frac{\partial \bar{p}}{\partial \lambda_a} = \left(\frac{1}{\lambda_a}\frac{\partial \mathcal{H}}{\partial \lambda_3} - \frac{\partial^2 \mathcal{H}}{\partial \lambda_a \partial \lambda_3}\right)\lambda_3 , \tag{21}$$

where λ_3 is a dependent value with regard to Eq. (9).

The presented formulation is valid for all incompressible membranous structures which are based on hyperelastic materials and form an essential general basis for subsequent sections.

2.3. Constitutive model problem of soft biological tissues

With the derived concept presented in previous sections the continuum framework only depends on the specification of one scalar function, i.e. the strain–energy density $\mathcal{H}$, the pursuit of which is the purpose of this section.

In this approach the non-linear stress–strain behavior of biological tissues is described with the most concise potential used in literature, i.e. the exponential potential proposed by Fung et al. [1] and Chuong and Fung [2, 3]

$$\mathcal{H}_{BIO} = c\{\exp[Q] - 1\} , \tag{22}$$

where c denotes a constant with the unit of pressure. Within the concept of finite bio-elastomechanics Q denotes a quadratic function of the components of the Green–Lagrangian strain tensor. A particular form for blood vessels might be chosen as

$$Q = a_1 E_1^2 + a_2 E_2^2 + a_3 E_3^2 + 2a_4 E_1 E_2 + 2a_5 E_2 E_3 + 2a_6 E_1 E_3 , \tag{23}$$

where $a_1, \ldots, a_6$ are non-dimensional constants characterizing the blood vessel and E_1, E_2 and E_3 denote the three Green–Lagrangian strain components in the circumferential, longitudinal and radial direction of, e.g. an artery, respectively; $E_{AB}(A \neq B)$ are assumed to be zero.

The theoretical prediction of the hydrostatic pressure follows from Eq. (16) using Eqs. (22), (23) and relation $2E_A = \lambda_A^2 - 1$, i.e.

$$\bar{p} = -\frac{2c}{(\lambda_1 \lambda_2)^2}[a_3 E_3 + a_5 E_2 + a_6 E_1]\exp[Q] . \tag{24}$$

The material coefficients $a_1, \ldots, a_6$ in the stored-energy function can be identified from a fitting process with the goal to minimize the errors between known experimental data and theoretical prediction.

If a blood vessel wall is treated as a membrane shell, only the average (uniform) strains in the circumferential (E_1) and longitudinal (E_2) direction are of interest. These simplified assumptions lead to the so-called two-dimensional approach, then, the analytical representation of $\mathcal{W}_{\text{BIO}}$, i.e. (22), (23), for a vessel segment is obtained merely by setting a_3, a_5 and a_6 to zero (see [1]). The alternative strain–energy function with four remaining material constants basically represents a 'compressible' material model in two dimensions.

The specification of the non-linear constitutive equation (17) and the consistent linearized tangent (20) results merely by computing the first and second derivative of $\mathcal{W}_{\text{BIO}}$ with respect to the principal stretches, i.e.

$$S_1 = 2c(a_1 E_1 + a_4 E_2)\exp[Q]\Big\} \atop S_2 = 2c(a_2 E_2 + a_4 E_1)\exp[Q]\Big\}, \qquad D = \begin{bmatrix} D_{11} & D_{12} \\ D_{21} & D_{22} \end{bmatrix}. \tag{25}$$

with

$$D_{11} = 2c\{a_1 + 2(a_1 E_1 + a_4 E_2)^2\}\exp[Q],$$

$$D_{22} = 2c\{a_2 + 2(a_2 E_2 + a_4 E_1)^2\}\exp[Q], \tag{26}$$

$$D_{12} = D_{21} = 2c\{a_4 + 2(a_1 E_1 + a_4 E_2)(a_2 E_2 + a_4 E_1)\}\exp[Q].$$

3. Finite element formulation

3.1. The principle of virtual work

With regard to a finite element concept the balance laws of a thin hyperelastic membrane are enforced in weak form. Therefore, we apply the principle of virtual displacements, in which the displacement field u is taken to be a fundamental unknown on the membrane surface $\partial\mathcal{B}_{0u}(u|_{\partial\mathcal{B}_{0u}} = \bar{u})$ of the boundary $\partial\mathcal{B}_0$ of the elastic continuum body.

Let $t := pn$ be defined as a normal traction vector on the membrane surface $\partial\mathcal{B}_{0u}$ with $\partial\mathcal{B}_0 = \partial\mathcal{B}_{0u} \cup \partial\mathcal{B}_{0\sigma}$ and $\partial\mathcal{B}_{0u} \cap \partial\mathcal{B}_{0\sigma} = \emptyset$. The load pressure p is a given constant per unit of the deformed differential surface element ds and n denotes the external unit normal vector field perpendicular to the loaded actual part $\partial\mathcal{B}_\sigma$. Further, if η denotes a vector of the virtual displacements, then, the weak form of the balance equation may be formulated by the stationary value of the functional $\mathcal{G}$, which is defined by

$$\mathcal{G}(u, \eta) := \underbrace{\int_{\partial\mathcal{B}_0} \delta E : SH \, dS}_{\delta\mathcal{W}_{\text{int}}} - \underbrace{\int_{\partial\mathcal{B}_\sigma} p\langle n, \eta\rangle \, ds}_{\delta\mathcal{W}_{\text{ext}}} = 0, \tag{27}$$

for any admissible variations η, which satisfying the mechanical boundary conditions $\eta|_{\partial\mathcal{B}_{0u}} = 0$. In Eq. (27) E and S are the corresponding strain and stress tensors for a membrane as discussed in Section 2.2. The two terms of $\mathcal{G}$ identified as $\delta\mathcal{W}_{\text{int}}$ and $\delta\mathcal{W}_{\text{ext}}$ denote the internal and external virtual work, respectively. The second term, $\delta\mathcal{W}_{\text{ext}}$ is the virtual work of the pressure on the boundary analyzed and extensively discussed by Schweizerhof and Ramm [35], Bufler [36] and with an application to axisymmetric problems given by Simo et al. [37].

By using a relation similar to Eq. (1)$_2$ for the current configuration and expressing the deformed differential surface element ds through the undeformed surface dS, the external virtual work of Eq. (27) may be rewritten to:

$$\underbrace{\int_{\partial\mathcal{B}_\sigma} p\langle n, \eta\rangle \, ds}_{\delta\mathcal{W}_{\text{ext}}} = \int_{\partial\mathcal{B}_{0\sigma}} \frac{p}{|G_1 \times G_2|} \langle g_1 \times g_2, \eta\rangle \, dS. \tag{28}$$

The non-linearity in u—caused both by the geometry and the material model—is implicitly present in the functional $\mathscr{G}(u, \eta)$. Therefore, with regard to an iterative algorithm of Newton's type, a consistent linearization of $\mathscr{G}$ at a known state u is necessary (see e.g. [38] or [31, Chs. 4–5]).

The linearization of the functional is obtained by

$$L\mathscr{G}(u, \eta, \Delta u) := \bar{\mathscr{G}} + \Delta\mathscr{G} + \cdots = 0, \tag{29}$$

where $\bar{\mathscr{G}}$ denotes constant and $\Delta\mathscr{G}$ linear terms, respectively. In this linearized problem the material linearization operator $\Delta\{\cdot\}$ (Gâteaux operator) is defined by the following rule (see [31, p. 185]):

$$\Delta\{\cdot\}(u, \eta, \Delta u) := D\{\cdot\}(u, \eta)\cdot\Delta u = \frac{\mathrm{d}}{\mathrm{d}\epsilon}\{\cdot\}(u + \epsilon\,\Delta u)\big|_{\epsilon=0}. \tag{30}$$

In view of the last two definitions (29) and (30) the functional $\mathscr{G}(u, \eta)$ together with Eq. (28) leads to:

$$\Delta\mathscr{G}(u, \eta, \Delta u) := D\mathscr{G}(u, \eta)\cdot\Delta u \equiv \int_{\partial\mathscr{B}_0}(\delta E : \Delta S + \delta\Delta E : S)H\,\mathrm{d}S$$

$$- \int_{\partial\mathscr{B}_{0\sigma}}\frac{p}{|G_1 \times G_2|}\langle[\Delta g_1 \times g_2 - \Delta g_2 \times g_1], \eta\rangle\,\mathrm{d}S = -\bar{\mathscr{G}}(u, \eta). \tag{31}$$

This linearized problem must be solved for the increments Δu until the residual $\bar{\mathscr{G}}(u, \eta)$ on the right-hand side of Eq. (31) vanishes within a prescribed tolerance.

3.2. Spatial discretization

The domain $\mathscr{B} \subset \mathbb{R}^n$ is divided in an arbitrary number of isoparametric finite elements of the form $\mathscr{B}^h = \mathbf{A}_{e=1}^{n_{elm}}\mathscr{B}^e$, where n_{elm} is the number of elements of the region and $\mathbf{A}$ denotes the assembly operator, respectively. With each single finite element, $\mathscr{B}^e \subset \mathscr{B}^h$, the position vector X, the displacement field u, the admissible variations η and the incremental displacements Δu are interpolated by the standard conventions of finite elements:

$$X \to X^h\big|_{\mathscr{B}^e} = \sum_{n=1}^{n_{nodes}^e} N_n X_n^e \qquad \eta \to \eta^h\big|_{\mathscr{B}^e} = \sum_{n=1}^{n_{nodes}^e} N_n q_n^e$$

$$u \to u^h\big|_{\mathscr{B}^e} = \sum_{n=1}^{n_{nodes}^e} N_n v_n^e \qquad \Delta u \to \Delta u^h\big|_{\mathscr{B}^e} = \sum_{n=1}^{n_{nodes}^e} N_n \Delta v_n^e \tag{32}$$

where the indicator h denotes the approximated function within the scope of an isoparametric concept. In Eq. (32), X_n, v_n, q_n, Δv_n ($n = 1, \ldots, n_{nodes}^e$) represent the nodal values of X^h, u^h, η^h, Δu^h, respectively. The number of nodes of a single element $\mathscr{B}^e$ is n_{nodes}^e and N_n are the isoparametric shape functions associated with nodes n.

In addition, we introduce the commonly used matrix B, containing derivatives of the shape functions. Then, the approximations for the virtual Green–Lagrangian strains δE and for the incremental strains ΔE yield:

$$\delta E \to \delta E^h\big|_{\mathscr{B}^e} = \sum_{n=1}^{n_{nodes}^e} B_n q_n^e$$

$$\Delta E \to \Delta E^h\big|_{\mathscr{B}^e} = \sum_{n=1}^{n_{nodes}^e} B_n \Delta v_n^e \tag{33}$$

With the above approximations, the discrete form of functional (29) is generated by

$$L\mathscr{G}^h(u, \eta, \Delta u)^h := \mathbf{A}_{e=1}^{n_{elm}}[\bar{\mathscr{G}}^h(v, q)\big|_{\mathscr{B}_0^e} + \Delta\mathscr{G}^h(v, q, \Delta v)\big|_{\mathscr{B}_0^e}] = 0. \tag{34}$$

For one finite element, Eq. (31) becomes:

$$\Delta \mathcal{G}^h(v, q, \Delta v)|_{\partial \mathcal{B}_0^\xi} := D\mathcal{G}^h(v, q)|_{\partial \mathcal{B}_0^\xi} \cdot \Delta v$$

$$\equiv \int_{\partial \mathcal{B}_0^\xi} (\delta E^h : \Delta S^h + \delta \Delta E^h : S^h) H \, dS^h$$

$$- \int_{\partial \mathcal{B}_{0\sigma}^\xi} \frac{p^h}{|G_1^h \times G_2^h|} \langle [\Delta g_1^h \times g_2^h - \Delta g_2^h \times g_1^h], \eta^h \rangle \, dS^h$$

$$= -\left[\int_{\partial \mathcal{B}_0^\xi} \delta E^h : S^h H \, dS^h - \int_{\partial \mathcal{B}_{0\sigma}^\xi} \frac{p^h}{|G_1^h \times G_2^h|} \langle g_1^h \times g_2^h, \eta^h \rangle \, dS^h \right], \tag{35}$$

where $\delta \Delta E^h$, ΔS^h and Δg_α^h are approximate linearized functions of the virtual strain tensor, the second Piola–Kirchoff stress tensor and the base vectors in the current configuration, respectively.

For a FE formulation a compact matrix notation will be used subsequently. With the help of relations (32), (33) and the assembling operator $\mathbf{A}$, the discrete functional given in Eq. (35) can be rewritten in a FE approximation as

$$\mathop{\mathbf{A}}_{e=1}^{n_{elm}} D\mathcal{G}^h(v, q)|_{\partial \mathcal{B}_0^\xi} \cdot \Delta v \equiv \mathop{\mathbf{A}}_{e=1}^{n_{elm}} \left(\sum_{n=1}^{n_{nodes}^e} \sum_{m=1}^{m_{nodes}^e} q_n^\mathrm{T} K_{nm}^e \Delta v_m \right)$$

$$= -\mathop{\mathbf{A}}_{e=1}^{n_{elm}} \left(\sum_{n=1}^{n_{nodes}^e} q_n^\mathrm{T} R_n^e \right). \tag{36}$$

Herein, K_{nm}^e is the tangent stiffness matrix for an element and is determined by the initial displacement matrix $B_n^\mathrm{T} D B_m$, the initial stress matrix $\tilde{K}_{nm}$ and the crucial load tangent stiffness matrix caused by deformation dependent loads, as follows:

$$K_{nm}^e := \int_{\partial \mathcal{B}_0^\xi} B_n^\mathrm{T} D B_m H \, dS^h + \tilde{K}_{nm} - \int_{\partial \mathcal{B}_{0\sigma}^\xi} \frac{p^h}{|G_1^h \times G_2^h|} N_n \sum_{p=1}^{p_{nodes}^e} (N_{p,1} N_{m,2} - N_{p,2} N_{m,1}) \tilde{x}_p \, dS^h, \tag{37}$$

where $N_{,\alpha}$ are the derivatives of the shape function N_n with respect to Θ^α and the known relation

$$\Delta v_m \times x_p = \tilde{x}_p \Delta v_m \quad \forall \Delta v_m \in \mathbb{R}^n \tag{38}$$

between the cross product and a skew-symmetric matrix $\tilde{x}_p$ has been used. Observe the 2×2 material matrix D of Eq. (37) which was explicitly presented by Eq. (20).

On the right-hand side of Eq. (36), R_n^e denotes the residual vector for the finite element which is defined by

$$R_n^e := \int_{\partial \mathcal{B}_0^\xi} B_n^\mathrm{T} S^h H \, dS^h - \int_{\partial \mathcal{B}_{0\sigma}^\xi} \frac{p^h}{|G_1^h \times G_2^h|} N_n \bar{g}_{12}^e \, dS^h, \tag{39}$$

where the first part denotes the stress divergence vector and the second part is the load vector including the deformation dependent loading terms. For convenience, in Eq. (39) we have introduced the definition

$$\bar{g}_{12}^e := g_1^h \times g_2^h = \sum_{n=1}^{n_{nodes}^e} \sum_{m=1}^{m_{nodes}^e} N_{n,1} N_{m,2} x_n \times x_m, \tag{40}$$

where x_n represents the nodal values of the current position vector x and S^h contains here the discrete second Piola–Kirchoff stress components obtained via the hyperelastic constitutive law, i.e. $S^h|_{\partial \mathcal{B}^e} = \sum_{n=1}^{n_{nodes}^e} DB_n v_n^e$.

Finally, for arbitrary virtual displacements $q \in \mathbb{R}^n$ a system of algebraic equilibrium equations follows from Eq. (36), which subsequently leads to the unknown corrector increments Δv.

4. Numerical examples

Finally, we focus on two characteristic problems from the field of physiological and medical research. The objective of the present section is to demonstrate the performance of the preceding formulation, the phenomenological model and the numerical efficiency of the proposed finite element implementation discussed above. A second main goal is to indicate a new practicable path for a numerical approach in the complex field of soft tissue mechanics. On the basis of a sound continuum formulation, the examples illustrate some novel numerical results on non-linear finite strain bio-elastomechanics using the finite element technique.

Due to the axisymmetric geometry of the test problems with known principal axes of deformation, an axisymmetric two-node membrane element was employed which ensures quadratic convergence behavior within the Newton–Raphson algorithm. For the developed finite elements which account for large membrane strains it is sufficient to discretize just the displacement field by linear interpolation functions (for more details on this subject see [37, 39]).

The constitutive model, the finite element formulation and the numerical algorithm for deformation dependent loadings have been implemented in the finite element program FEAP, developed by R.L. Taylor and J.C. Simo (see [40] for a documentation).

4.1. Inflation of a prestrained blood vessel—rat aorta

The first example investigates the non-linear mechanical behavior of an abdominal aorta from a male Wistar rat via FE method. For the experimental set-up employed in this investigation and for a detailed discussion of the analytical assumptions and framework, the reader may be referred to [41–43] with more references therein. With regard to a numerical simulation it seems to be important to give a rough explanation of the experimental process.

Basically, an aorta segment cannulated at one end and closed at the other was inserted between the clamps of a tensile testing machine and stretched to several levels of successive lengths. At each length the blood vessel, which is connected to a piston pump is inflated with a static pressure from 0 up to 200 mm Hg (mercury) (26.66 kPa) acting along the luminal wall. For a certain longitudinal stretch ratio λ_z and an applied pressure p, measurements were made for the outer diameter d and the axial force. In addition, the outer diameter D and the wall-thickness H of the undeformed configuration of the vessel segment were measured. The experimental results are reported in [43].

A straightforward computation with the incompressibility condition (9) (assumption that the arterial wall deforms iso-volumetrically) leads to the current wall thickness, i.e. $h = H/\lambda_z\, D/d$. Subsequently, within an analytical framework, which basically results from the equilibrium condition of thin pressure vessels, the non-linear stress–strain relationship can easily be computed. The results for the physiological axial prestretch, which is approximately $\lambda_z = 1.60$ are given in Figs. 1 and 2 and denoted as 'experimental'.

As a next step the experimental stress–strain curves were fitted with a non-linear least-squares algorithm over all experimental data points for $\lambda_z = 1.60$. The material parameters obtained were $c = 0.61163 \cdot 10^5$ Pa, $a_1 = 0.68238$, $a_2 = 0.60558$ and $a_4 = 0.61163$, with $a_3 = a_5 = a_6 = 0$, which goes along with the two-dimensional approach discussed in Section 2.3. The obtained coefficients minimize the sum of squares of the difference between known experimental data and predicted theoretical results. The fitted curves, labeled as 'theoretical' are presented in Figs. 1 and 2.

Based on these material coefficients the numerical simulations were performed with only one axisymmetrical membrane element and the specific geometry 0.122 mm (wall-thickness) and 1.648 mm (outer diameter) for the load free (undeformed) configuration was employed (see [43]).

The first loading procedure, the prestrained state for $p = 0$ ($\lambda_z = 1.60$) was simulated followed by a second loading process which increases the pressure with incremental values of $\Delta p = 10$ mm Hg up to 200 mm Hg, see Figs. 1 and 2. Therein, the radial displacements on the ends of the vessels are unlocked and for the inflation test the tube was fixed in a longitudinal direction. Note that the inner pressure is always normal to the surface, which significantly changes during the simulation. Since the stiffness changes due to the deformation dependent loads (see third term in Eq. (37)), large load steps can also
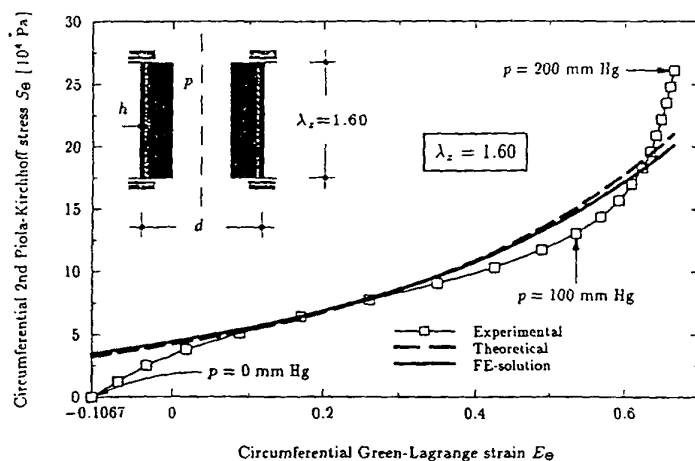
Fig. 1. Inflation of a prestrained blood vessel: circumferential second Piola–Kirchhoff stress S_θ versus circumferential Green–Lagrange strain E_θ at $\lambda_z = 1.60$, experimental data, theoretical and finite element solution.
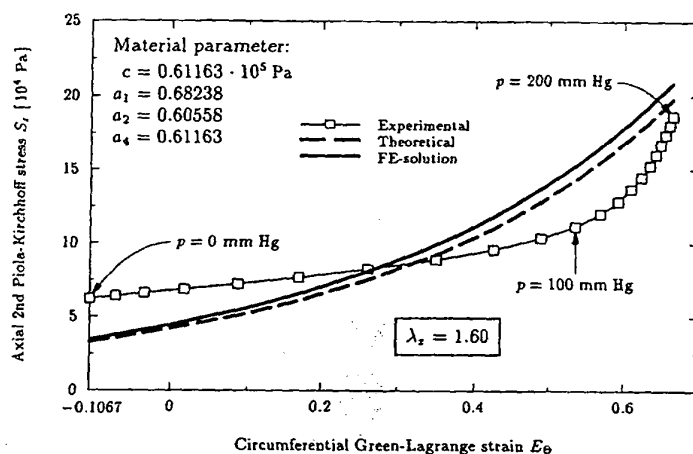

Fig. 2. Inflation of a prestrained blood vessel: axial second Piola–Kirchhoff stress S_z versus circumferential Green–Lagrange strain E_θ at $\lambda_z = 1.60$, experimental data, theoretical and finite element solution.

Table 1
Inflation of a prestrained blood-vessel: norms of the residual for a typical increment load $\Delta p = 10$ mm Hg—showing quadratic convergence behavior

Iteration	Step 1 (90→100 mm Hg)	Step 2 (100→110 mm Hg)
1	4.49923×10^{-02}	4.58039×10^{-02}
2	3.79605×10^{-03}	3.48725×10^{-03}
3	2.17250×10^{-05}	1.65929×10^{-05}
4	7.22517×10^{-10}	3.80461×10^{-10}

be considered and a quadratic convergence of the unbalanced forces near the solution point is always achieved—for two characteristic load steps see Table 1.

REMARK 6.1. The non-linear stress–strain relationships (Figs. 1 and 2) show qualitatively good agreement with the theoretical values which motivates to discretize geometrically more complex problems (like bifurcations) found in the field of tissue engineering. This is a task for future work.

However, as seen in Fig. 1 the experimental stress–strain relationship of a prestrained abdominal aorta is typically 'S-shaped', which cannot be replicated with the employed strain–energy function of exponential form. A potential which is capable to simulate the *overall* pressure domain more accurately was recently proposed by Weizsäcker et al. [27, 28]. This new potential for elastic and muscular arteries is composed of a neo-Hookean potential and an anisotropic potential as used in this paper. It allows a representation of the 'biphasic' behavior of arteries for the first time. An implementation of the improved structure of the constitutive model within the general concept presented in Section 2 appears to be straightforward, the goal of a followup paper. □

4.2. *Contact of a balloon catheter with an atherosclerotic artery*

The last example is concerned with the mechanics of balloon angioplasty occurring in clinical applications.

Percutaneous transluminal angioplasty (PTA) follows the primary role to enlarge the luminal (cross-sectional) area of a chronic atherosclerotic blood vessel by inducing and inflating a (latex) balloon dilatation catheter, leading to decreased resistance to blood flow. However, dilatation catheters generate increases of intramural stresses and strains, which also depend on the catheter design (see e.g. [44]). The most damage during balloon angioplasty occurs to the intima and media (see [45]), which can give rise to *restenosis* and *embolic symptoms* (luminal thrombosis)—overzealous dilatation can damage the contractile function of the smooth-muscle cells (see e.g. [46] among many others). One aim of the angioplasty technique is to produce controlled injury with a predictable healing response [47]. For further details regarding the general characteristics of PTA, the standard references by Becker et al. [48], Veith et al. [49], Chs. 21–22 are recommended.

There has been only a few investigations into the mechanics of balloon angioplasty published in the literature (see e.g. [46, 50]). Analytical solutions of the non-linear mechanics of balloon angioplasty involving relatively complex geometry are hardly available, experiments are often difficult to perform. An efficient FE approach, which can handle the contact of a tiny balloon-tipped catheter with an artery narrowed by fatty deposits is one goal of this example—to the author's knowledge still not available in the literature. Another purpose of the present study is to contribute to the knowledge in the mechanics of this complex process associated with finite strain elasticity by visualizing the global deformation behavior of the structure and the intramural stresses.

Our attention is restricted to fully axisymmetrical problems of the model atherosclerotic vessel and the balloon catheter. Geometry and material parameter of the blood vessel—an abdominal aorta of a male Wistar rat—are adopted from the first example. The artery segment with a length of 2.5 mm was discretized by 50 axisymmetrical finite elements and prestrained up to 4.0 mm with a simulation process according to the first example, then, the current diameter for the middle surface becomes 1.353 mm and the wall-thickness is 0.086 mm.

The centric plaque has a lumen with radius $R_1 = 0.39$ mm, as illustrated in Fig. 3. Furthermore, the assumption was made that the idealized plaque in the middle of the artery is circularly shaped with radius $R_2 = 0.28$ mm and the total length of the stenosis is 3.8 mm with a thickness on both ends of 0.01 mm. The plaque geometry of an idealized model stenosis was discretized by 500 axisymmetrical finite deformation elements, which are based on a mixed FE formulation and a Hadamard material model. Basically, the compressible case of the neo-Hookean material was used, for further details see [51]. The mixed formulation circumvents the well-known locking response for the incompressible limit observed by a pure displacement formulation. The stress-free centric plaque is assumed to rest frictionless on the artery wall.

Little attention has been paid to the biomechanical properties of atherosclerotic tissues, which can
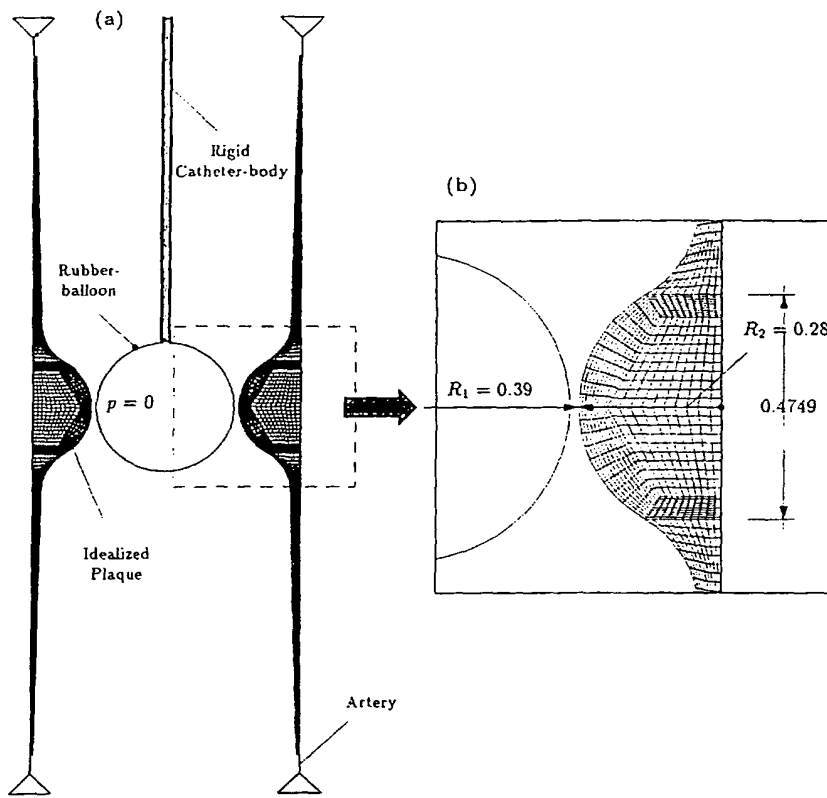
Fig. 3. Contact of a balloon catheter with an atherosclerotic artery: discretization of an idealized atherosclerotic artery cross section with a balloon catheter showing the prestrained (reference) configuration. There are 650 axisymmetric elements: 50 artery. 500 plaque and 100 catheter (a); close-up view of the discretized centric model plaque (dimensions in millimeter) (b).

significantly vary from specimen to specimen, from hard to soft. Artery plaque systems behave as non-linear elastic under the high stresses imposed by a percutaneously introduced balloon catheter. Very little experimental data regarding non-linearity, homogeneity and compressibility of the plaque within the physiological range are available (see e.g. [52]). The determination of material properties is still an area of incomplete knowledge and always produces controversial opinions among scientists. For our simulations the assumption was made that the biomaterial of the atherosclerotic plaque is elastic and isotropic, described with typical value, i.e. the static shear modulus $G = 500 \, \text{N}/\text{m}^2$ and the bulk modulus $\kappa = 724.6 \, \text{N}/\text{m}^2$ (see [53, 54] for further details). Observe that the plaque generally is more rigid than the artery wall and most resistant to deformation. The strength of material composition of the dilatation balloon, which is held within a rigid catheter body as seen in Fig. 3, has to be sufficient to exert the pressure on areas of stenosis. For our simulations we have chosen a sphere with the diameter of the middle surface of 0.70 mm and a wall-thickness of 0.10 mm, which was discretized by 100 axisymmetrical membrane elements. The catheter is modeled with the classical Mooney–Rivlin material (see [8]) which is adopted from empirical rubber-elasticity. The employed isotropic potential reads: $\mathcal{W} = \Sigma_{\alpha=1}^2 \, b_\alpha (I_\alpha - 3)$, where the positive constants are chosen to be $b_2/b_1 = 1/3.225$ and I_α denote the principal invariants of $\hat{C}$ as described in Eq. (4).

Fig. 3 shows the system of the prestrained artery completely restrained at both ends with the cross section of the idealized plaque and the catheter, which is assumed to be the reference configuration. This is the point of departure for exertion of the dilating pressure on the stenosis. The atheromatous plaque is pressurized by the membrane surface of the balloon. The contact constraint is enforced by

means of a classical penalty method. The deformed shapes of the diseased vessel and the catheter with contour plots of radial Cauchy stresses in the plaque are displayed in Fig. 4 for a final state of the process (intraballoon pressure $p = -2.05\,\text{N/mm}^2$, maximum contact pressure $\sigma_1 = -0.419\,\text{N/mm}^2$). The elastic catheter-plaque system which is pressed into contact by the applied pressure of the catheter give rise to a Hertzian contact pressure distribution, clearly seen in Fig. 5.

Finally, the constitutive relations used have been implemented in a non-linear axisymmetrical quasi-Kirchhoff-type shell element, which is based on a formulation presented by Eberlein et al. [55]. An analog contact simulation of the geometrical and physical non-linear behavior of the system were performed, which remarkably showed almost identical results.

REMARK 6.2. It has to be mentioned that the final solution of this analysis will strongly depend upon the constitutive model used, which is probably the most poorly understood part in soft tissue mechanics and continually one goal of research. Implementations of efficient damage models are without doubt a next unalterable refinement towards a satisfactory constitutive modeling of vascular disorders.

In future, 'computer aided balloon angioplasty' may help to predict indications for operations more precisely and may represent a method which enables different more efficient therapeutical interventions. Certainly the long-term goal of computer simulations of this important and very attractive clinical technique will be an aid to restrict occurrences of restenosis and to avoid difficulties by surgery which increases the rate of success for the treated patients.

In this sense the present numerical study which is relevant to medicine should be considered as a basis for further needed research on the computational treatment of vascular surgery. □
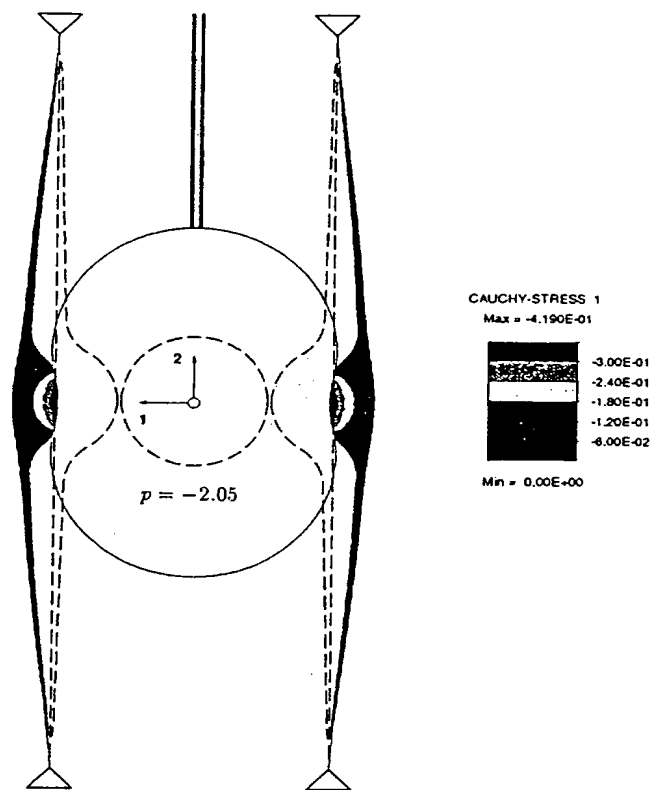

Fig. 4. Contact of a balloon catheter with an atherosclerotic artery: deformed configuration of the balloon dilated atherosclerotic wall for the final state, showing Cauchy stresses in radial direction (dashed lines indicate the prestrained reference configuration).

CAUCHY-STRESS 1
Max = -1.190E-01

-3.00E-01
-2.40E-01
-1.80E-01
-1.20E-01
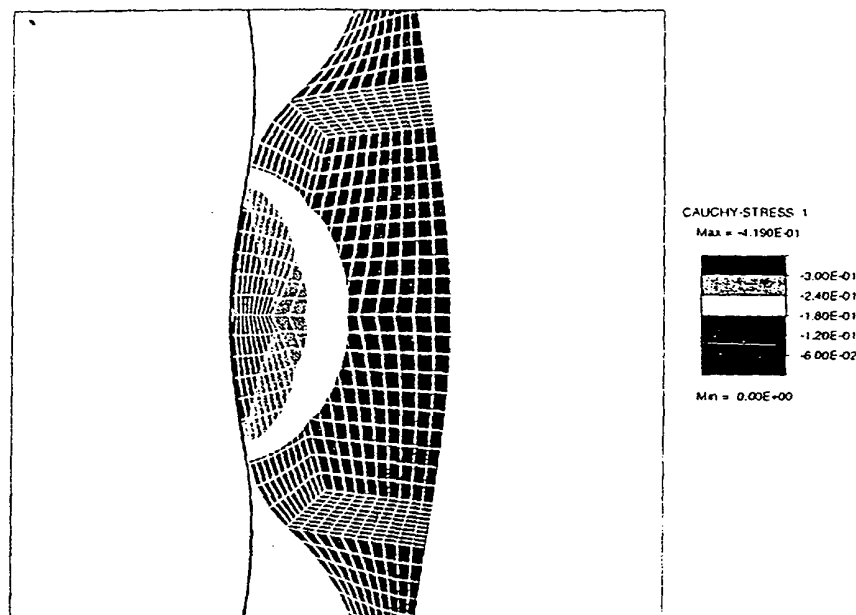-6.00E-02

Min = 0.00E+00

Fig. 5. Contact of a balloon catheter with an atherosclerotic artery: close-up view of the deformed system for the final state, showing the Hertzian contact pressure distribution in the plaque (Cauchy stresses in radial direction).

5. Conclusion

In the present paper a classical constitutive model for biotissues has been employed to describe the highly non-linear stress response of homogeneous and incompressible hyperelastic thin membranes—in particular of blood vessels. The condition of incompressibility has been imposed by a relation which expresses the radial deformation of the membrane through the in-plane (tangential) deformations. The assumption of a plane stress state has been enforced by introducing a potential through a Lagrangian multiplier (identified with pressure), which was explicitly determined. Derivatives of the strain–energy function with respect to Green–Lagrangian strains have led to the stresses and the elasticity tensor for an incompressible membrane. This framework is exclusively provided in a geometric setting relative to the reference configuration and encompasses a wide range of phenomenologically based hyperelastic constitutive models. To describe the perfectly elastic deformation behavior of soft biological (arterial) tissues, a particularization was carried out.

On the basis of approximate displacement fields, a non-linear FE formulation for the finite strain behavior has been derived. A consistent linearization procedure of the governing equations allows the possibility to use large load steps by following quadratically convergent equilibrium iterations. Consequently, the developed finite elements are very efficient and, in general, applicable for various materials in the large strain range.

The performance of the described formulation and the accuracy of the numerical results have been demonstrated for two representative biomedical examples. For the first time in literature we were able to numerically simulate the mechanics of balloon angioplasty within the context of a FE method. The relevant information recorded in this study has been the connection between the applied internal pressure of the balloon catheter (loading) and the global deformation behavior of the structure (effect). The long-term trend in vascular surgery can be seen in accompanying computer-aided analyses which will help to visualize complex (patho-)physiological processes with the goal to minimize the risks for the treated patients.

Acknowledgments

References

[1] Y.C. Fung, K. Fronek and P. Patitucci, Pseudoelasticity of arteries and the choice of its mathematical expression. Am. Physiol. Soc. 237 (1979) H 620–H 631.

[2] C.J. Chuong and Y.C. Fung, Three-dimensional stress distribution in arteries, Trans. ASME 105 (1983) 268–274.

[3] C.J. Chuong and Y.C. Fung, Compressibility and constitutive equation of arterial-wall in radial compression experiments. J. Biomech. 17 (1984) 35–40.

[4] D.H. Bergel, The properties of blood vessels, in: Y.C. Fung, N. Perrone and M. Anliker, eds., Biomechanics: Its Foundations and Objectives (Prentice-Hall, Englewood Cliffs, NJ, 1972) 105–139.

[5] P.B. Dobrin, Vascular mechanics, in: J.T. Shepherd and F.M. Abboud, eds., Handbook of Physiology. Section 2: The Cardiovascular System, Vol. III (Am. Physiol. Soc., Bethesda, Maryland, 1983) 65–102.

[6] H.W. Weizsäcker and J.G. Pinto, Isotropy and anisotropy of the arterial wall. J. Biomech. 21 (1988) 477–487.

[7] M. Mooney, A theory of large elastic deformation. J. Appl. Phys. 11 (1940) 582–592.

[8] R.S. Rivlin, Large elastic deformations of isotropic materials. I–IV, Phil. Trans. R. Soc. Lond. Ser. A 240 (1948) 459–525 and A241 (1948) 379–397.

[9] D.J. Patel and D.L. Fry, The elastic symmetry of arterial segments in dogs. Circulation Res. 24 (1969) 1–8.

[10] T.E. Carew, R.N. Vaishnav and D.J. Patel, Compressibility of the arterial wall. Circulation Res. 23 (1968) 61–68.

[11] Y.C. Fung, Rheology of blood vessels, in: G. Kaley and B.M. Altura, eds., Microcirculation 1 (University Park Press, Baltimore, 1977) 299–324.

[12] M.R. Roach and A.C. Burton, The reason for the shape of the distensibility curves of arteries. Can. J. Biochem. Physiol. 35 (1957) 681–690.

[13] D.A. McDonald, Blood Flow in Arteries, 3rd edition (Edward Arnold Publishers Ltd., 1974).

[14] Y.C. Fung, S.Q. Liu and J.B. Zhou, Remodeling of the constitutive equation while a blood vessel remodels itself under stress. J. Biomech. Engrg. 115 (1994) 453–459.

[15] J. Zhou, Theoretical analysis of bending experiments on aorta and determination of constitutive equations of materials in different layers of arterial walls. Dissertation, University of California, San Diego, CA, 1992.

[16] Y.C. Fung, Biomechanics: Motion, Flow, Stress, and Growth (Springer, New York, 1990).

[17] J.P. Xie, S.Q. Liu, R.F. Yang and Y.C. Fung, The zero-stress state of rat veins and vena cava. J. Biomech. Engrg. 113 (1991) 36–41.

[18] R.N. Vaishnav and J. Vossoughi, Estimation of residual strain in aortic segments, in: C.W. Hall, ed., Biomedical Engineering II. Recent Developments (Pergamon Press, 1983).

[19] K. Hayashi, H. Handa, K. Mori and K. Moritake, Mechanical behavior of vascular walls. J. Soc. Mater. Sci. Japan 20 (1971) 1001–1011.

[20] K. Takamizawa and K. Hayashi, Strain energy density function and uniform strain hypothesis for arterial mechanics. J. Biomech. 20 (1987) 7–17.

[21] K. Hayashi, Experimental approaches on measuring the mechanical properties and constitutive laws of arterial walls. J. Biomech. Engrg. 115 (1993) 481–488.

[22] D.J. Patel and R.N. Vaishnav, The rheology of large blood vessels, in: D.H. Bergel, ed., Cardiovascular Fluid Dynamics, Vol. 2 (Academic Press, New York, 1972) 1–64.

[23] R.N. Vaishnav, J.T. Young and D.J. Patel, Distribution of stresses and of strain–energy density through the wall thickness in a canine aortic segment. Circulation Res. 32 (1973) 577–583.

[24] R.L.R. Wesly, R.N. Vaishnav, J.C.A. Fuchs, D.J. Patel and J.C. Greenfield Jr., Static linear and non-linear elastic properties of normal and arterialized venous tissue in dog and man. Circulation Res. 37 (1975) 509–520.

[25] Y.C. Fung, Biorheology of soft tissues, Biorheology 10 (1973) 139–155.

[26] H. Demiray, H.W. Weizsäcker, K. Pascale and H.A. Erbay, A stress–strain relation for a rat abdominal aorta. J. Biomech. 21 (1988) 369–374.

[27] H.W. Weizsäcker, G.A. Holzapfel and G.W. Desch, A biphasic potential for arteries, in: K. Häkkinen, K.L. Keskinen, P.V. Komi and A. Mero, eds., Proc. XVth Cong. of the Internat. Soc. Biomech., Jyväskylä, Finland, July 2–6, 1995, pp. 988–989.

[28] H.W. Weizsäcker, G.A. Holzapfel, G.W. Desch and J.G. Pinto, Constitutive equation for elastic and muscular arteries, in: M. Singh and V.P. Saxena, eds., Advances in Physiological Fluid Dynamics. Proc. 4th Internat. Conf. Physiol. Fluid Dynamics and 2nd Internat. Conf. Clinical Haemorheology, Jiwaji University, Gwailior, India, December 8–10, 1995 (Narosa Publishing House, New Delhi, 1966) 21–25.

[29] B.R. Simon, M.A. Kaufmann, M.A. McAfee and A.L. Baldwin, Finite element models for arterial wall mechanics, J. Biomech. Engrg. 115 (1993) 489–496.

[30] C. Truesdell and W. Noll, The non-linear field theories of mechanics, in: S. Flügge, ed., Encyclopedia of Physics, Vol. III/3 (Springer, Berlin, 1965).

[31] J.E. Marsden and T.J.R. Hughes, Mathematical Foundations of Elasticity (Dover Publications, New York, 1994).

[32] R.W. Ogden, Non-linear Elastic Deformations (Ellis Horwood, Chichester, 1984).

[33] B. Budiansky, Notes on non-linear shell theory, J. Appl. Mech. 35 (1968) 393–401.

[34] Y.C. Fung, Foundations of Solid Mechanics (Prentice-Hall, Englewood Cliffs, NJ, 1965).

[35] K.H. Schweizerhof and E. Ramm, Displacement dependent pressure loads in non-linear finite element analysis, Comput. Struct. 18 (1984) 1099–1114.

[36] H. Buffer, Pressure loaded structures under large deformations, Z. Angew. Math. Mech. 64 (1984) 287–295.

[37] J.C. Simo, R.L. Taylor and P. Wriggers, A note on finite-element implementation of pressure boundary loading, Comm. Appl. Numer. Methods 7 (1991) 513–525.

[38] T.R.J. Hughes and K.J. Pister, Consistent linearization in mechanics of solids and structures, Comput. Struct. 8 (1978) 391–397.

[39] P. Wriggers and R.L. Taylor, A fully non-linear axisymmetrical membrane element for rubber-like materials, Engrg. Comput. 7 (1990) 303–310.

[40] O.C. Zienkiewicz and R.L. Taylor, The Finite Element Method, 4th edition, Vol. 1 (McGraw-Hill, London, 1989).

[41] H.W. Weizsäcker, H. Lambert and K. Pascale, Analysis of the passive mechanical properties of rat carotid arteries, J. Biomech. 16 (1983) 703–715.

[42] H.W. Weizsäcker, Passive elastic properties of the rat abdominal vena cava. Pflügers Arch. 412 (1988) 147–154.

[43] H.W. Weizsäcker and T.D. Kampp, Passive elastic properties of the rat aorta. Biomed. Technik 35 (1990) 224–234.

[44] T.B. Kinney, A.K. Chin, G.W. Rurik, J.C. Finn, P.M. Shoor, W.G. Hayden and T.J. Fogarty, Transluminal angioplasty: A mechanical-pathophysiological correlation of its physical mechanism, Radiology 153 (1984) 85–89.

[45] C.L. Zollikofer, E. Salomonowitz, R. Sibley et al., Transluminal angioplasty evaluated by electron microscopy. Radiology 153 (1984) 369–374.

[46] P.M. Consigny, T.N. Tulenko and R.F. Nicosia, Immediate and long-term effects of angioplasty-balloon dilation on normal rabbit iliac artery, Arteriosclerosis 6 (1986) 265–276.

[47] Y. Korogi and M. Takahashi, Light and electron microscopic observations in atherosclerotic rabbits following experimental transluminal angioplasty, Acta Radiologica 28 (1987) 323–328.

[48] G.J. Becker, B.T. Katzen and M.D. Dake, Noncoronary angioplasty, Radiology 170 (1989) 921–940.

[49] F.J. Veith, R.W. Hobson, R.A. Williams and S.E. Wilson, Vascular Surgery. Principles and Practice, 2nd edition (McGraw-Hill, New York, 1994).

[50] P.C. Block, Mechanism of transluminal angioplasty, Am. J. Cardiology 53 (1984) 69c–71c.

[51] J.C. Simo and K.S. Pister, Remarks on rate constitutive equations for finite deformation problems: Computational implications, Comput. Methods Appl. Mech. Engrg. 46 (1984) 201–215.

[52] G.V.R. Born and P.D. Richardson, Mechanical properties of human atherosclerotic lesions, in: S. Glagov, W.P. Newman and S.A. Schaffa, eds., Pathophysiology of the Human Atherosclerotic Plaque (Springer, New York, 1990) 413–423.

[53] H.M. Loree, R.D. Kamm, R.G. Stringfellow and R.T. Lee, Effects of fibrous cap thickness on peak circumferential stress in model atherosclerotic vessels, Circulation Res. 71 (1992) 850–858.

[54] R.M. Jones, Macromechanical behavior of a lamina, in: Mechanics of Composite Materials (McGraw-Hill, New York, 1975) 31–57.

[55] R. Eberlein, P. Wriggers and R.L. Taylor, A fully non-linear axisymmetrical quasi-Kirchhoff-type shell element for rubber-like materials, Int. J. Numer. Methods Engrg. 36 (1993) 4027–4043.

XP-001014246

Échographie endocoronaire et angioplastie

Summary

Endocoronary Ultrasonography and Angioplasty.

G. Finet*

At the end of the 20th century, endocoronary ultrasonography has become established in many catheter laboratories. The information provided by this technique of invasive imaging has many qualitative and quantitative features. Is endocoronary ultrasonography a research or an everyday clinical tool to be used systematically or occasionally in routine procedures ?

Endocoronary ultrasonography is really a research tool because it is not redundant with conventional coronary angiography. Ultrasonography investigates the whole arterial wall. Its spatial resolution is twice that of angiography. Its contribution in this field is rich with many reports on arterial modelling, post-angioplasty remodelling, plaque rupture and atherothrombosis, the accurate description of the mechanical effects of angioplasty tools, two and three-dimensional quantification of atherosclerotic plaques and, finally, providing a very accurate biomechanical approach.

Its use in routine procedures is only occasionally justified as there is no scientific proof in favour of a more widespread use with respect to changing the procedure or to evaluating patient prognosis.

Endocoronary ultrasonography, a very rich technique, should be available in all catheter laboratories for occasional use.

This technique is useful for all cardiologists performing coronary angioplasty by improving the evaluation of atheromatous plaques and countering the intrinsic ambiguities of coronary angioplasty. Arch Mal Cœur 1999 ; 92 : 1681-9.

Résumé

À la veille de l'an 2000, l'échographie endocoronaire est entrée dans de nombreux laboratoires de cathétérisme cardiaque. Les informations fournies par cette technique d'imagerie invasive présentent de grandes qualités qualitatives et quantitatives. L'échographie endocoronaire est-elle un outil de recherche ou un outil clinique à utiliser systématiquement ou occasionnellement en routine ?

Elle est réellement un outil de recherche puisqu'il est non redondant avec l'angiographie coronaire par rayons X. L'échographie explore toute la paroi artérielle. Sa résolution spatiale est 2 fois supérieure à celle de l'angiographie. Sa contribution dans ce domaine est riche avec de nombreux résultats sur le modelage artériel, le remodelage après angioplastie, les ruptures de plaque et l'athérothrombose, la description précise des effets mécaniques des outils utilisés, les quantifications bidimensionnelles ou tridimensionnelles de la plaque d'athérosclérose, et enfin une approche biomécanique extrêmement précise.

Son utilisation en routine ne peut être qu'occasionnelle puisqu'il n'existe actuellement aucun élément scientifique suffisamment démonstratif pour autoriser une utilisation plus systématique en vue de changer soit nos procédures soit le pronostic de nos patients.

L'échographie endocoronaire, technique d'une grande richesse, devrait être présente dans chaque laboratoire de cathétérisme pour une utilisation occasionnelle en routine.

Cette technique est utile pour chaque angioplasticien en enrichissant sa perception de la plaque d'athérosclérose et en levant les ambiguïtés intrinsèques de l'angiographie coronaire. Arch Mal Cœur 1999 ; 92 : 1681-9.

(*) Service d'hémodynamique, hôpital cardiovasculaire L.-Pradel, BP Lyon-Monchat, 69394 Lyon Cedex 03.
(Tirés à part : Pr G.Finet).

L'imagerie échographique endocoronaire est devenue, à la veille de l'an 2000, une technique d'imagerie mature. Les artères coronaires ne peuvent être explorées que de manière invasive. Deux techniques

sont actuellement disponibles : l'angiographie par rayons X et l'échographie endovasculaire. L'imagerie des artères coronaires par échographie endovasculaire est bien différente de l'imagerie obtenue par rayons X. Il s'agit d'une imagerie en temps réel, à haute résolution, tomographique, de la lumière et de la paroi artérielle. La question que l'on est en droit de se poser actuellement est la suivante : l'échographie endocoronaire est-elle uniquement un outil de recherche ou un outil clinique de routine ? En d'autres termes, son utilisation est-elle indispensable, pour la conduite diagnostique ou thérapeutique de nos patients, en laboratoire de cathétérisme cardiaque ?

Pour tenter de répondre à cette question, nous présentons la méthode d'utilisation actuelle de l'échographie endocoronaire et nous tenterons d'apporter les réponses à ces questions au cours de la discussion.

MÉTHODES

Acquisition

La taille des cathéters à ultrasons disponible à l'heure actuelle va de 2,8 à 3 french, les fréquences employées varient entre 30 et 40 Mhz. Les cathéters à rotation mécanique sont plus utilisés que les cathéters

électroniques. Effectivement, le meilleur critère de qualité des cathéters est représenté par la surface du transducteur, environ 0,8 mm², la puissance du faisceau ultrasonore émise est proportionnelle au carré de cette surface d'émission. Une miniaturisation excessive diminue en corollaire la puissance acoustique, principal déterminant de la qualité des images échographiques. Cependant, la qualité des cathéters électroniques progresse. Les cathéters actuels sont compatibles 6F.

Toutes les procédures d'exploration échographique exigent l'injection préalable de 250 mg d'aspirine, et d'un bolus de 2 000 unités d'héparine. L'injection de dinitrate d'isosorbide ou de molsidomine doit être réalisée systématiquement avant la procédure. Le cathéter à ultrasons est amené au-delà du segment artériel que l'on désire explorer, sous contrôle radiologique, au niveau d'une zone précise et facilement reproductible telle qu'une bifurcation artérielle distale. Le retrait doit être rendu automatique par l'utilisation d'un système autorisé assurant la régularité du retrait et sa quantification. Une donnée quantitative longitudinale est ainsi possible. Cette donnée intervient dans toutes les analyses volumiques quantitatives, dans la pertinence d'une reconstruction tridimensionnelle, et dans le repérage artériel nécessaire à la reproductibilité de la
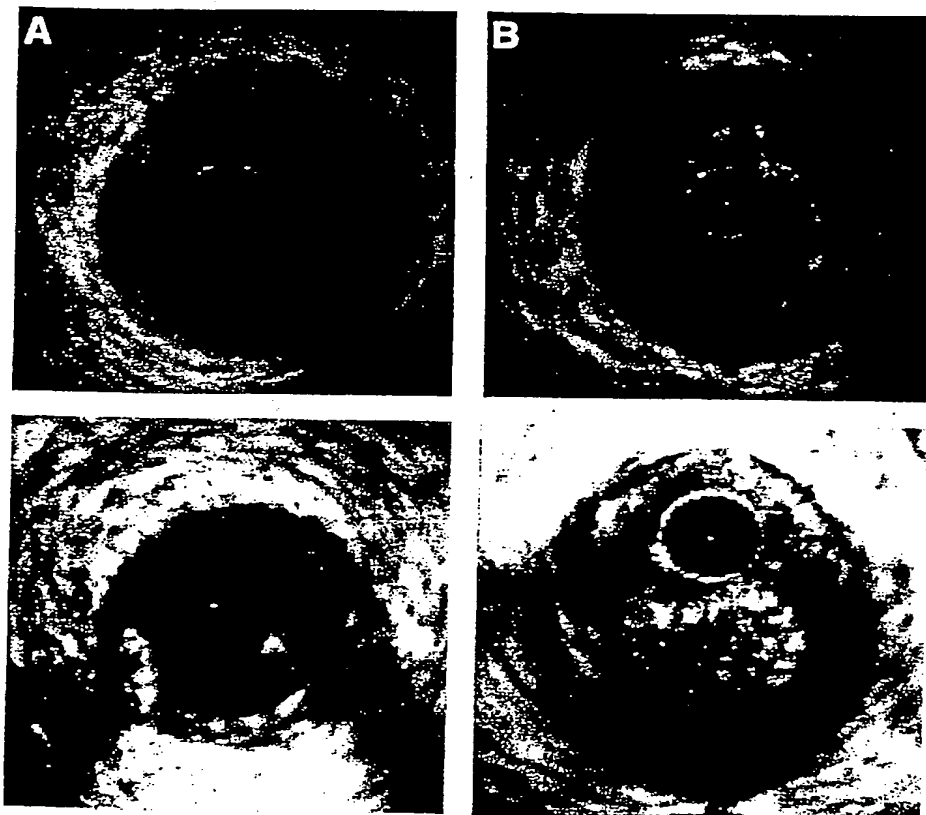

FIG. 1 - Différents aspects échographiques de la plaque d'athérosclérose coronaire. A : aspect échographiquement normal d'une artère coronaire avec l'aspect typique en 3 couches caractérisant la limitante élastique interne, soulignant la média, et caractérisant le port adventiciel. B : plaque fibrocellulaire excentrée. Il est impossible sur des données échographiques de savoir si le contenu anéchogène est lipidique ou cellulaire (spumeux, inflammatoire, ou dérivé de produits sanguins). C : plaque fibrocalcaire excentrée. D : plaque ulcérée avec rupture centrale de la plaque et comblement par un thrombus qui remplit la niche formée par la rupture de plaque.

FIG. 1 - Different ultrasonic images of coronary atherosclerotic plaques. A: normal appearances of a coronary artery with three layers characterising the internal elastica underlying the media and the adventica. B: excentric fibrocellular plaque. It is impossible to determine from an ultrasonic imaging if the anechogenic component is lipid or cellular (spumous, inflammatory or blood products). C: excentric fibro-calcific plaque. D: ulcerated plaque with central rupture filled with thrombus.

mesure d'un segment particulier, à 2 temps différents de l'exploration. Toute ambiguïté qualitative sur l'image du contour endoluminal, induite par la rétrodiffusion acoustique du sang, doit être levée par l'injection à fort débit d'un bolus de sérum salé isotonique au travers du cathéter-guide.

Traitement qualitatif de l'image

L'artère coronaire échographiquement normale est représentée par un aspect caractéristique en 3 couches, dont l'épaisseur est à peu près constante, de 300 µm environ. La détection d'une plaque d'athérosclérose est facile à identifier sur les images échographiques. La texture de l'image échographique permet de distinguer 3 composants principaux (fig. 1). Une échogénicité modérée et homogène caractérise une structure de nature fibreuse. Une hyperéchogénicité avec atténuation du faisceau ultrasonore traduit une zone calcaire, il peut y avoir quelquefois ambiguïté avec une fibrose dense de type hyaline. Une zone hypo- ou anéchogène traduit une structure cellulaire. Elle n'est donc pas synonyme de zone lipidique. L'hypoéchogénicité ou anéchogénicité traduit l'absence de réflecteur acoustique. Il s'agit donc d'une structure riche en eau. Le contenu est donc lipidique (extracellulaire) ou cellulaire (cellules spumeuses, cellules inflammatoires, produits sanguins). Nous avons décrit précédemment les ambiguïtés diagnostiques propres à l'interprétation qualitative de l'image échographique endocoronaire [1].

Analyse quantitative

Deux contours peuvent être tracés sur une image échographique endocoronaire : le contour endoluminal et le contour artériel total. Le contour endoluminal consiste à suivre le bord d'attaque de l'écho engendré par l'interface sang-paroi artérielle. La détection de ce contour est le plus souvent réalisable sans grande difficulté mais quelques problèmes spécifiques peuvent apparaître [2]. Le cathéter à ultrasons est souvent en position excentrée au contact de la paroi et peut gêner la détection de cette surface qui disparaît du fait du contact avec le cathéter. D'autre part l'échogénicité du sang, surtout à 40 Mhz, peut être telle que les impédances acoustiques du sang et de la paroi deviennent très proches. La visualisation de l'interface disparaît alors, gênant la détection du contour. Une telle situation apparaît principalement lorsque le flux sanguin est ralenti, ce qui favorise la formation de rouleaux d'hématies, dont l'importance croît de manière inversement proportionnelle à la vitesse du sang. Ces rouleaux deviennent alors des réflecteurs acoustiques importants et gênent ainsi considérablement le traçage des contours endoluminaux. Une méthode simple permet d'améliorer la détection visuelle de ce contour endoluminal et consiste à enlever les réflecteurs sanguins en injectant au travers du cathéter porteur un bolus de sérum salé isotonique à fort débit. L'utilisation de produit de contraste acoustique est aussi une solution [3].

Le second contour est le contour artériel total et correspond au traçage effectué en dedans du bord d'attaque de l'écho produit par l'interface média, limitante élastique externe et adventice. Le traçage de ce contour est généralement facile mais peut dans certains cas être partiellement absent. Cette disparition localisée du contour est due aux zones d'absence de transmission des faisceaux ultrasonores par des composants hyper-réflecteurs de la plaque. Ces composants sont les plaques fibreuses denses et les plaques calcaires. Il convient alors d'extrapoler ce contour en fonction du contour visible en s'aidant des images adjacentes à celle sur laquelle on effectue les mesures. Au total 2 tracés sont réalisés et fournissent 2 contours. Ces 2 contours créent 2 surfaces : la surface endoluminale et la surface artérielle totale. La différence de ces 2 surfaces fournit la surface intima + média ou plaque + média. Au total, 3 surfaces sont ainsi obtenues par 2 traçages de contour. Il importe de détecter les déformations géométriques engendrées par les changements de position du cathéter ultrasons au sein de l'artère explorée. L'ensemble de ces traitements quantitatifs doit être disponible sur une station de travail informatique dédiée, conviviale et interactive (logiciel IVUS Iô3.2, IôDP, Paris). La reconstruction tridimensionnelle et la visualisation (fig. 2) offrent un potentiel majeur dans l'analyse quantitative volumique [4]. L'analyse des artefacts de formation de cette imagerie tridimensionnelle est réalisée afin d'assurer la validité des informations [5].

FIG. 2 - Reconstruction tridimensionnelle d'une sténose serrée de l'interventriculaire antérieure proximale avec visualisation d'une branche latérale (première septale). La texture de l'image échographique est conservée sur ce type de reconstruction permettant une analyse longitudinale de cette plaque fibro-cellulaire.
FIG. 2 - Three-dimensional reconstruction of a severe proximal LAD stenosis with visualisation of a lateral branch (first septal). The texture of the ultrasonic image is preserved in this type of reconstruction, enabling longitudinal analysis of this fibrocellular plaque.

Pièges dans l'interprétation des images

L'image échographique peut présenter des artefacts, autrement dit des aspects spécifiques, produits par le système d'imagerie qui ne reflètent pas la réalité [6, 7]. Ces pièges sont surtout induits par des artefacts formés sur l'image échographique endovasculaire lors de l'exploration des stents. Les stents, structures métalliques, sont hyperéchogéniques. Leur visualisation sur l'image est donc particulièrement bien visible. C'est parce qu'elles sont bien visibles que ces structures ont été largement exploitées et ont rendu semble-t-il l'échographie endovasculaire indispensable lors du déploiement de ces prothèses. L'échographie endovasculaire semble ainsi bénéfique en évitant les implantations insuffisantes, les défauts d'apposition des filaments sur la paroi artérielle, et enfin en fournissant des données quantitatives afin d'optimiser la taille du ballon et des pressions d'inflation [8-10]. Cependant, plusieurs points critiques apparaissent. Depuis l'introduction de l'échographie endovasculaire, la plupart des
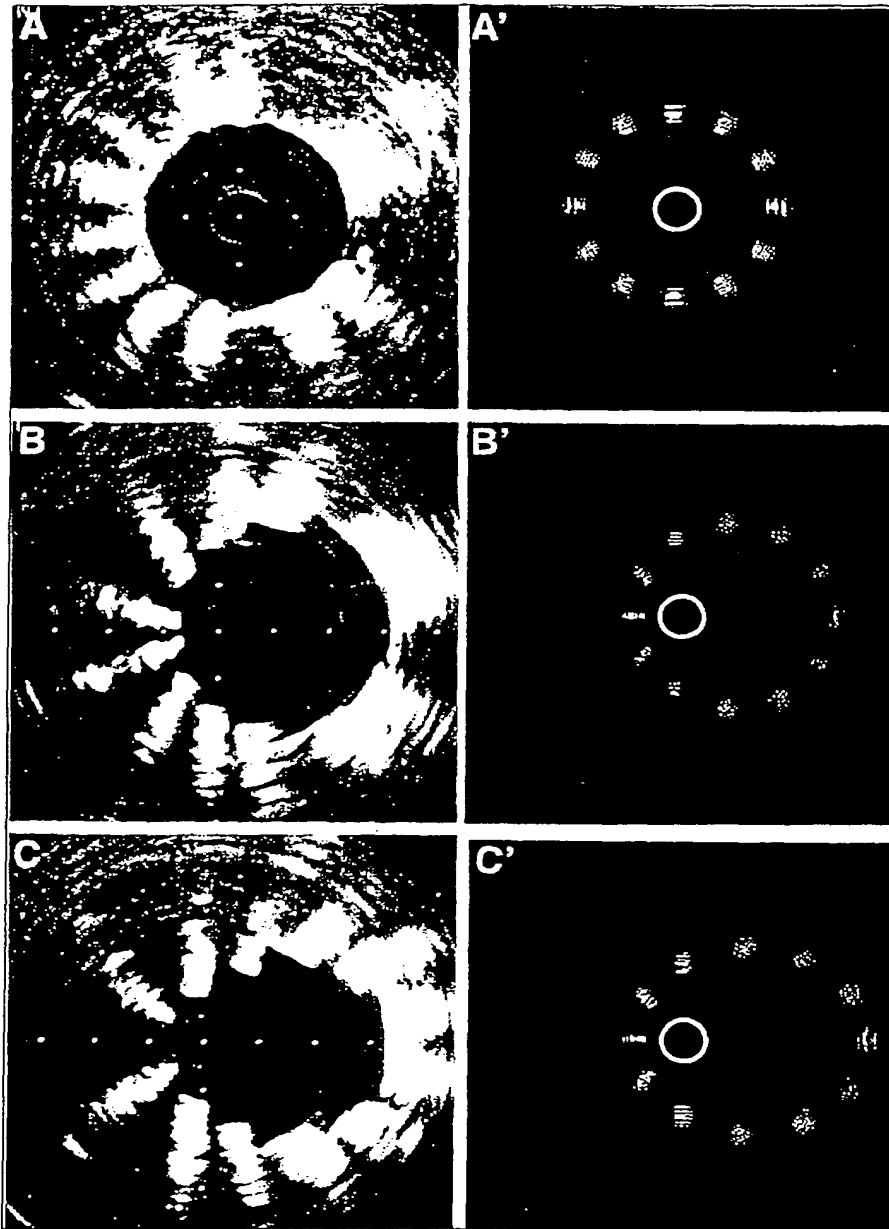

FIG. 3 - Démonstration des artefacts caractéristiques de l'exploration échographique endovasculaire des endoprothèses coronaires. A gauche, les images sont acquises in vitro, sur le même stent (Palmaz Schatz - PS 154) déployé à un diamètre très précis de 4 mm. A droite, l'image est issue d'une simulation numérique complète d'un stent virtuel déployé à un diamètre de 4 mm. A : le transducteur ultrasonore est centré, les contours sont parfaitement circulaires, l'interprétation est optimale, les quantifications sont justes. B : le cathéter est excentré au contact du stent mais l'axe longitudinal du cathéter est parallèle à l'axe longitudinal de l'artère. Le stent n'est que peu déformé globalement, cependant, les échos des filaments deviennent obliques pour certains d'entre eux et la largeur de ces échos varie en fonction de la distance qui les sépare du transducteur. L'analyse qualitative peut être ainsi perturbée et les quantifications sont modérément altérées. C : le transducteur est incliné de 30 ° à l'intérieur du stent. Une déformation géométrique typique en ellipse apparaît. S'y associe les variations de largeur des échos des filaments et leur changement d'orientation. L'ensemble de ces modifications sur l'image altère significativement l'interprétation que l'on peut avoir sur l'implantation du stent et modifie profondément les quantifications.

FIG. 3 - Demonstration of characteristic artefacts of endovascular ultrasonic imaging of coronary stents. On the left, the appearances acquired in vitro of the same stent (Palmaz Schatz - PS 154) expanded to a very precise diameter of 4 mm. On the right, an image from total numeric stimulation of a virtual stent expanded to 4 mm. A: the ultrasonic transducer is centred, the contours are perfectly circular, the interpretation is optimal and quantification is accurate. B: the catheter is ex-centred in contact with the stent but the longitudinal axis of the catheter is parallel to the longitudinal axis of the artery. The stent is only slightly deformed globally ; however, the echoes of the filaments become oblique and the width of these echoes varies according to the distance between them and the transducer. Qualitative analysis can be affected and quantification may be approximate. C: transducer inclination at 30° within the stent. Typical ellipsoid deformation. Associated variations in the width of the echoes of the filaments and change in orientation. The changes significantly alter the interpretation of the stent implantation and greatly affect the quantification.

stents déployés (85 % environ) paraissent mal implantés. Ces mauvaises implantations semblent fondées sur plusieurs éléments propres aux images échographiques : une géométrie asymétrique du stent à l'origine de sections elliptiques [8, 9], des filaments obliques, dont le nombre caractériserait une expansion asymétrique du stent [9], une géométrie parfois complexe en forme de pétale où les filaments semblent converger vers le transducteur [8, 11], et enfin des défauts d'apposition de certains filaments contre la paroi artérielle [8, 9]. Malheureusement, plusieurs paradoxes apparaissent dans la littérature et ne sont pourtant pas mis en exergue. Pourquoi tous les défauts d'implantation ne peuvent être corrigés ou prévenus par une implantation guidée par l'échographie endovasculaire ? Pourquoi malgré l'utilisation de hautes pressions d'inflation ou de ballons de diamètre supérieur, les critères échographiques initialement retenus en faveur d'un défaut de déploiement sont ils toujours présents ?

Nous avons analysé les interactions complexes qui lient les filaments métalliques des stents et leurs dispositions géométriques tridimensionnelles avec les propriétés acoustiques du cathéter à ultrasons et sa position en réalisant des études expérimentales *in vitro* et des simulations numériques complètes (fig. 3) [12, 13]. L'échographie endovasculaire apparaît globalement comme une technique d'imagerie relativement inadaptée à l'exploration sérieuse des stents. Effectivement, l'interprétation des images échographiques omet complètement les principes de formation de cette image : position intraluminale ultrasonore, rotation du faisceau ultrasonore et interaction acoustique entre les filaments et le transducteur. Tous ces éléments sont à l'origine d'artefacts qui perturbent nos interprétations qualitatives et altèrent significativement nos quantifications. Il apparaît ainsi logique d'être confronté à des discordances étonnantes entre les données échographiques et angiographiques.

DISCUSSION

Une discussion sur l'échographie endovasculaire doit s'articuler autour de 2 questions : l'échographie endocoronaire est-elle un outil de recherche ou est-elle un outil clinique à réaliser au quotidien [14].

Outil de recherche ?

L'échographie est certainement un outil de recherche de grande qualité puisqu'il est essentiellement non redondant avec la seule imagerie que l'on peut utiliser pour l'exploration des artères coronaires : l'angiographie par rayons X. L'échographie explore toute la paroi artérielle ce que ne fait pas l'angiographie. Elle fournit des données quantitatives 2 fois plus précises que l'angiographie (90 μm versus 200 μm) [7, 15]. Ces 2 propriétés rendent cet examen indispensable pour l'exploration *in vivo* de l'artère normale et surtout de la plaque d'athérosclérose. D'autre part, l'échographie associe l'analyse morphologique de la plaque (bidimensionnelle ou tridimensionnelle) et l'analyse relativement précise de sa composition : ces 2 caractéristiques sont observées en condition de charge physiologique. L'apport est considérable sur nos connaissances de l'évolution de la plaque d'athérosclérose, sur le modelage et le remodelage post-angioplastie de cette plaque. Nous avons acquis la connaissance de 2 modelages ou remodelages caractéristiques : la dilatation artérielle dite compensatrice décrite initialement par Glagov et coll.[16] et la constriction artérielle chronique. Cet aspect bimodal du modelage artériel a été décrit tant après angioplastie que sur des artères coronaires natives [17, 18]. Nous avons pu montrer que ces 2 modelages ne sont pas exclusifs et coexistent très souvent (fig. 4, page suivante) [12]. De plus, le phénomène de constriction artérielle, initialement retrouvé dans le remodelage post-angioplastie dans 25 % environ des cas est présent de manière focale ou globale dans plus de 75 % des sténoses coronaires (fig. 5, page suivante). Les connaissances nouvelles ont fortement contribué à modifier notre perception de la plaque d'athérosclérose et ont eu des impacts importants : compréhension de l'existence d'angiogrammes normaux alors que l'athérosclérose est déjà diffuse, critique sur la quantification angiographique de l'athérosclérose, critique sur les segments de référence lors de la quantification des sténoses, amélioration dans la compréhension de l'action des outils d'angioplastie. L'échographie peut nous fournir dans certaines occasions anatomiques des informations sur l'adventice, tunique fort importante dans les modelages précédemment décrits, et qui subit elle aussi un modelage pathologique. Nous avons pu montrer que l'adventice en rapport avec l'existence d'une plaque peut avoir une épaisseur jusqu'à 4 fois supérieure à celle d'une adventice d'artère normale [19]. L'échographie s'est révélée beaucoup plus sensible dans la détection des calcifications [20] et plus précise dans la détermination et la quantification des lésions coronaires. Elle s'est avérée donc une méthode de choix pour l'évaluation des sténoses avant et surtout après angioplastie. De plus, plusieurs études ont démontré que l'échographie endovasculaire permettait une détection précoce de l'athérosclérose accélérée du greffon en visualisant un épaississement intimal des vaisseaux coronaires angiographiquement normaux chez les patients explorés à intervalles réguliers après une transplantation cardiaque. L'analyse relativement fine de la composition de la plaque à permis de montrer que dans l'angor instable, les patients avaient moins de plaques hyperéchogènes fibrocalcaires (10 %) et beaucoup plus de plaques à dominance cellulaire (90 %) donc potentiellement riches en lipides et en cellules inflammatoires. La détection des ruptures spontanées ou de l'athérothrombose est un avantage certain de l'imagerie échographique endovasculaire.

L'échographie comme outil de recherche permet d'aller plus loin dans l'extraction des données avec en particulier une analyse des comportements biomécaniques de la plaque d'athérosclérose directement visualisés chez le patient. Cela est le fruit d'un travail en collaboration avec des biomécani-
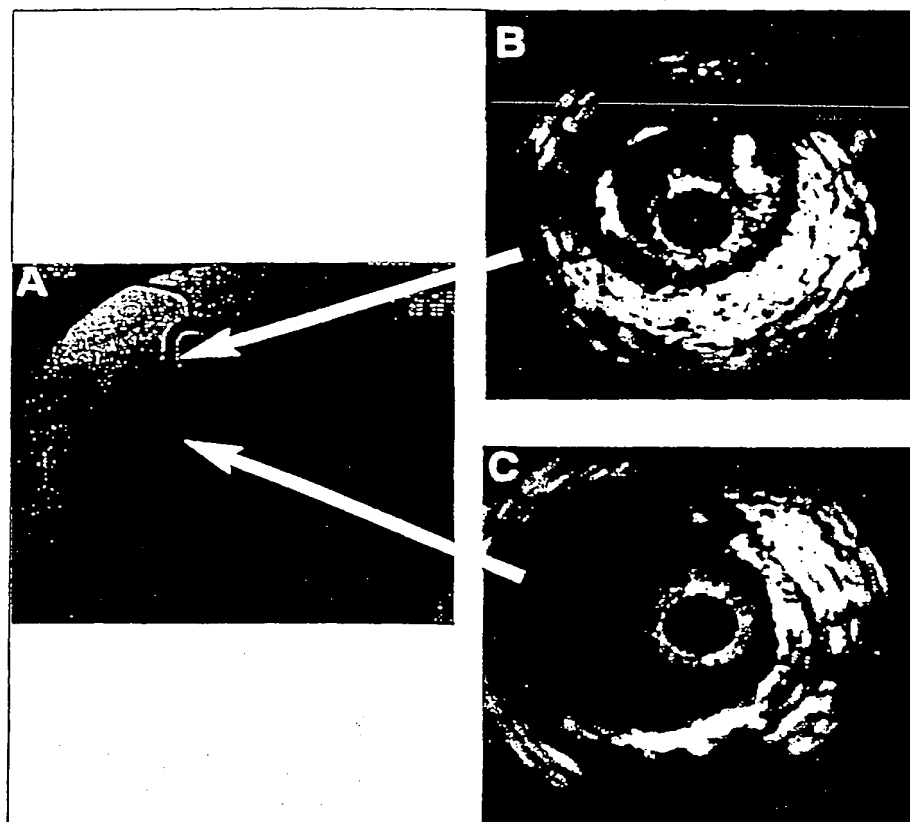
FIG. 4 - Exemple de remodelage constrictif artériel. A : angiogramme d'une coronaire droite où l'on peut voir un aspect ampullaire sur le deuxième segment de cette artère. B : coupe échographique sur le segment proximal adjacent à l'ampoule : phénomène de modelage constrictif chronique majeur avec réduction de 40 % de la taille totale de l'artère. C : coupe échographique endocoronaire au niveau de l'ampoule. Aspect subnormal avec épaississement fibreux intimal excentré. La masse athéroscléreuse est identique dans ces 2 cas. Le processus sténosant global des segments adjacents à l'ampoule n'est donc induit que par un processus constrictif et non par un épaississement athéroscléreux.

FIG. 4 - Examples of constrictive arterial remodelling. A: Angiogramme of a right coronary artery with the ampullary appearances of the second segment. B: ultrasonic section of the segment proximal to the ampulla : phenomenon of chronic constrictive modelling with 40% reduction of the total lumen of the artery. C: Endocoronary ultrasonography at the ampulla. Subnormal appearances with eccentric fibrous intimal thickening. The atherosclerotic mass is the same in the two cases. The stenotic process of the adjacent segments to the ampulla is only induced by a constrictive process, not by athrosclerotic thickening.

ciens. Ces travaux biomécaniques nous apportent des éléments riches d'informations sur la vulnérabilité de la plaque d'une part et sur les forces compressives que l'artère fait subir à une éventuelle endoprothèse (fig. 6). Enfin, l'analyse volumique, permise grâce à l'échographie endovasculaire, permet des analyses très fines de la plaque d'athérosclérose ou de la prolifération néo-intimale intras-
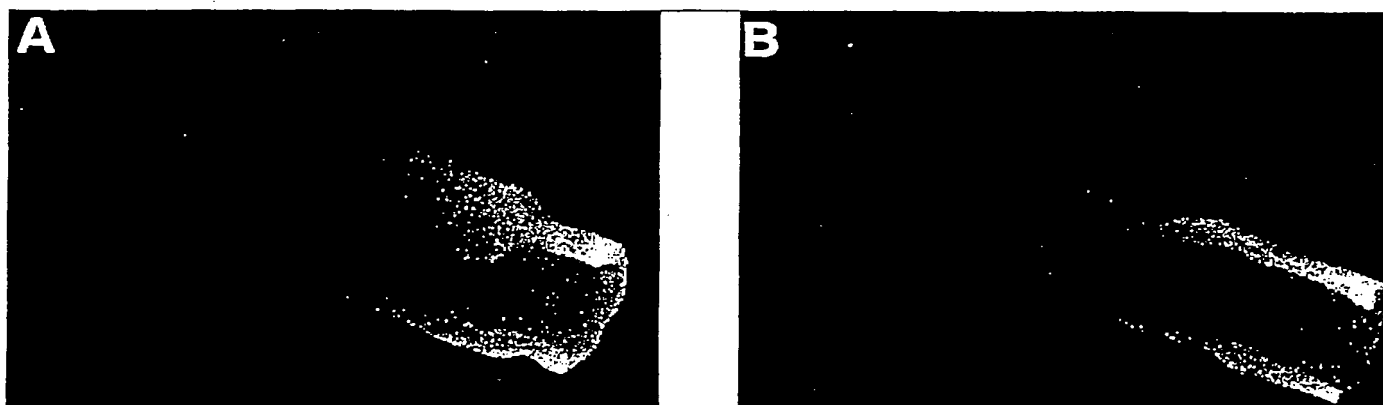

FIG. 5 - Aspect bimodal des modelages de 2 sténoses coronaires athéroscléreuses natives. A : dilatation compensatrice défaillante puisque le processus a malgré tout abouti à la formation d'une sténose endoluminale. B : constriction artérielle chronique globale particulièrement bien objectivée. Ces 2 lésions sont des lésions sténosantes serrées de 2 artères interventriculaires antérieures. Il s'agit de reconstruction tridimensionnelle in vivo.
FIG. 5 - Bimodal appearance of modelling of two native atherosclerotic coronary stenoses. A: inadequate compensatory dilatation as the process has resulted in the formation of endoluminal stenosis. B: chronic global arterial constriction, particularly well demonstrated. These two lesions are severe stenoses of the left anterior descending arteries. This is an in-vivo three-dimensional reconstruction.

tent (fig. 7, page suivante). Plusieurs grands travaux sur la progression ou régression de la plaque d'athérosclérose sous statine vont commencer en utilisant la quantification volumique après reconstruction tridimensionnelle de la plaque d'athérosclérose sur un long segment artériel à des temps d'évolution différents.

L'échographie endovasculaire est donc un remarquable outil de recherche, non redondant, précis, reproductible, et dont la contribution durant ces 5 dernières années a été réellement considérable.

Imagerie clinique de routine ?

La question que l'on doit se poser pour la pratique quotidienne de l'échographie est la suivante : l'échographie doit-elle être réalisée systématiquement en cours d'angioplastie ou occasionnellement. En d'autres termes, existe-t-il actuellement des éléments scientifiques qui nous obligent à réaliser cette technique pour modifier directement, et pour chaque patient, une thérapeutique ou un éventuel pronostic [21].

L'échographie est-elle nécessaire pour sélectionner les outils d'angioplastie ? De nombreuses études largement dominées par les travaux du *Washington Hospital Center*, préconisent l'utilisation systématique de l'échographie avant angioplastie pour choisir l'outil adapté à la lésion traitée [22]. Les résultats cliniques qui en découlent ne sont guère probants, ils ne modifient ni le résultat ni le pronostic des patients. Ils sont à l'origine d'une augmentation du temps de procédure, ils sont souvent liés à l'utilisation de cathéters à 8 à 10 french pour permettre l'utilisation de tous les outils disponibles. Que dire d'une méthode aussi lourde alors qu'en France par exemple, nous réalisons nos angioplasties en 6F, avec de très faibles doses d'héparine (2 500 UI), ballon et stent (dans 80 % des procédures), une ablation immédiate de l'introducteur, et le tout avec une temps de procédure de 25 min environ. Le taux de thrombose aiguë ou subaiguë est inférieur à 1,5%.

L'échographie est-elle prédictive de la resténose ? Les études sont très divergentes et ambiguës [22-25].
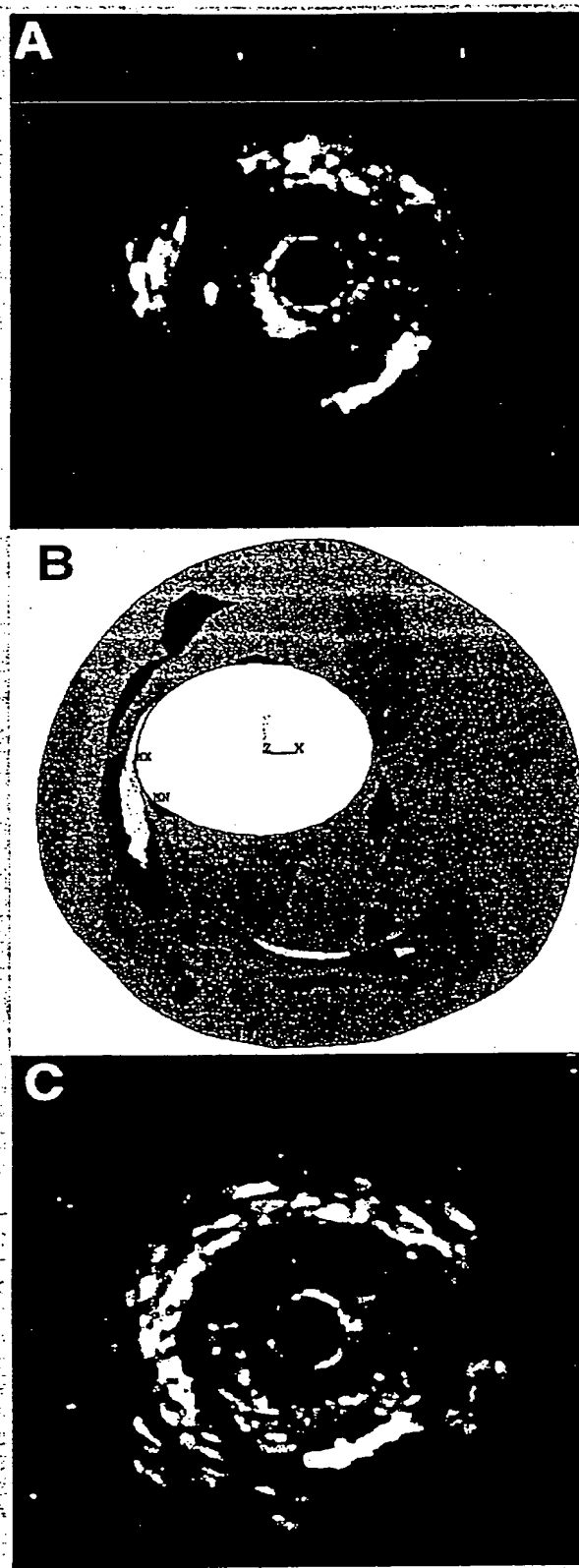

FIG. 6 - Analyse *in vivo* biomécanique du comportement de la plaque d'athérosclérose grâce à l'association de l'échographie endocoronaire et de l'analyse par les éléments finis. A : image d'une plaque fibro-calcaire avant angioplastie. B : cartographie des contraintes de cisaillement où apparaît une importante zone de contrainte maximale partant de la lumière et se prolongeant vers la plaque calcaire. Il s'agit d'une zone potentielle de rupture si les contraintes appliquées à l'artère deviennent supérieures aux contraintes de rupture des éléments fibreux constituant la plaque. C : l'image échographique après angioplastie objective une rupture de plaque. Cette rupture était parfaitement prévisible sur les images de cartographie biomécanique.
FIG. 6 - In-vivo biomechanical analysis of the atherosclerotic plaque by the association of endocoronary ultrasonography and analysis of the elements. A: image of a fibro-calcified plaque before angioplasty. B: mapping of the shearing stress showing a zone of maximal stress extending from the lumen to the calcified plaque. It is a zone of potential rupture if the stresses on the artery become greater than the stress of rupture of the fibrous elements of the plaque. C: ultrasonographic imaging after angioplasty showing plaque rupture. This rupture was perfectly predictable from the biomechanical mapping data.
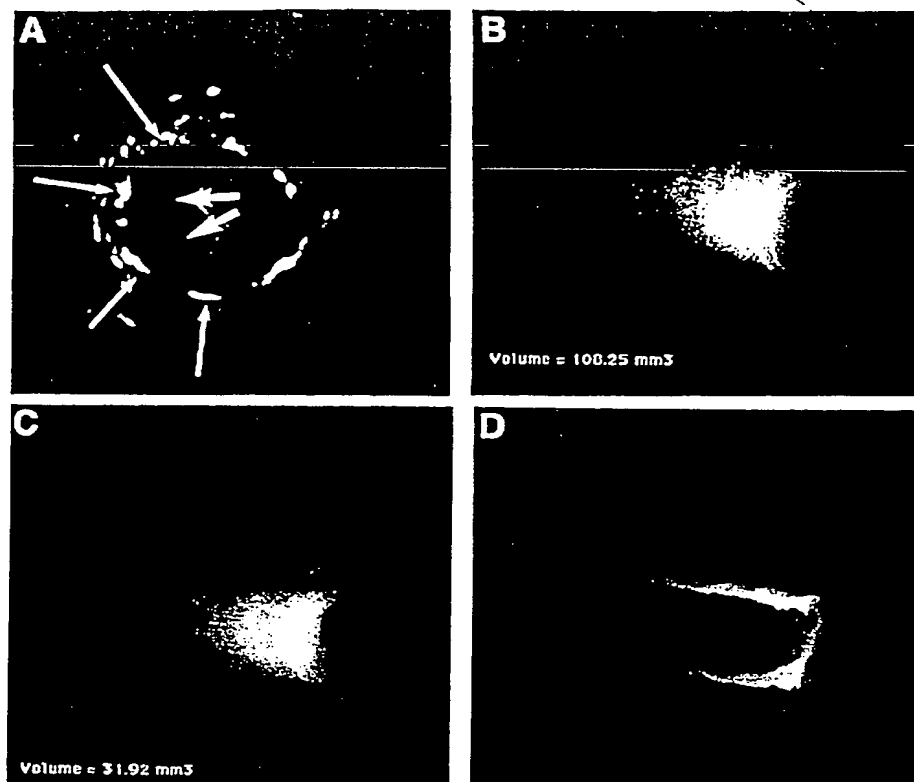
FIG. 7 - Exemples d'analyses quantitatives volumiques par échographie endocoronaire d'une prolifération néo-intimale à l'intérieur d'un stent tubulaire. A : une vue échographique bidimensionnelle de la prolifération néo-intimale. B : reconstruction volumique tridimensionnelle du volume intrastent. C : volume après reconstruction tridimensionnelle de la prolifération néo-intimale à l'intérieur du stent. D : d'après découpage électronique longitudinal de cette prolifération, il est possible d'en apprécier l'uniformité de la répartition au sein de ce stent.

FIG. 7 - Examples of quantitative volumic analyses of endocoronary ultrasonography of neo-intimal proliferation with a tabular stent. A: two-dimensional ultrasonic appearances of neo-intimal proliferation. B: Three-dimensional volumic reconstruction of intra-stent volume. C: volume after three-dimensional reconstruction of neo-intimal proliferation within the stent. D: after longitudinal electronic section of this proliferation, the uniformity of the distribution of this proliferation within the stent may be observed.

L'importance de la plaque résiduelle après angioplastie et les importantes dissections semblent être des facteurs prédictifs de resténose. D'autres études ne retrouvent aucun critère prédictif significatif [26, 27]. Si nous étions capables de prédire une éventuelle resténose, le problème qui se poserait à nous serait de savoir qu'elle serait alors notre action thérapeutique spécifique. Il n'y en a pas donc cette prédiction n'a guère d'intérêt en routine clinique.

L'échographie est-elle un indicateur précis de bonne implantation des stents? Ce grand sujet apparu en 1994 repose sur l'intérêt potentiel de l'échographie endocoronaire pour l'optimisation du déploiement des endoprothèses fondée à partir de critères issus des images échographiques réalisées lors de l'implantation [28]. Certains auteurs ont observé que dans plus de 80 % des cas, les stents étaient mal implantés [8]. Il y a donc discordance apparente entre l'aspect angiographique et l'aspect échographique [29]. Cela est un premier paradoxe. La réaction immédiate à cette observation a été d'utiliser des ballons de taille supérieure ou surtout de plus haute pression d'inflation. Les hautes inflations sont nées. Alors, un deuxième paradoxe est apparu. Ce paradoxe est décrit dans quasiment toutes les publications importantes et souligne le fait que les critères qui ont servi à la description d'une mauvaise implantation sont systématiquement retrouvés après l'utilisation de hautes pressions d'inflation. Nous avons pu expliquer puis démontrer par simulation numérique

que l'hyperéchogénicité des filaments est à l'origine de nombreux artefacts qui modifient très sensiblement notre interprétation et aussi les quantifications. Ce que nous voyons sur l'image n'est pas le stent ou les filaments mais les échos du stent ou des filaments. La forme de ces échos est très particulière et les déformations géométriques induites par les déplacements du cathéter sont à l'origine de toutes ces déformations. Il est donc bien normal de retrouver ces mêmes critères quelle que soit la surinflation imposée au stent. Quatre-vingt-quinze pour cent des études présentées utilisent toujours le même stent : le Palmaz-Schatz. Nous avons pu montrer aussi par simulation numérique que la pression d'inflation nécessaire pour ce stent est d'environ 14 bars, elle est donc en accord avec la littérature en général [30]. Mais cette pression n'est pas du tout applicable à l'ensemble des stents dont les propriétés mécaniques sont bien différentes. Il n'y a pas de pression magique mais une pression d'inflation à adapter en fonction du ballon utilisé (pression nominale du ballon), de la pression de déploiement du stent et de son recoil élastique intrinsèque (propriétés mécaniques du stent) qui doit être compensé par une surinflation déterminée d'après les courbes compliance fournies par le constructeur. Enfin, Schiele et coll., au moyen d'une belle étude randomisée comparant 2 groupes d'angioplastie avec implantation de stents guidés ou non guidés par échographie endocoronaire, ne trouvent aucune différence significative en terme de resténose [31].

CONCLUSION

L'échographie endocoronaire est une technique d'imagerie invasive qui nous fournit des informations d'une grande précision, complètes, et non redondantes si on les compare à l'angiographie coronaire. C'est avant tout un outil de recherche dont les résultats ont fortement contribué à modifier notre perception de la plaque d'athérosclérose. L'échographie ne peut être à l'heure actuelle un outil d'imagerie réalisé au quotidien et systématiquement au cours des procédures interventionnelles. Il est coûteux et surtout aucun résultat probant ne nous conforte dans l'idée qu'il faille appliquer cette technique à tous nos patients au cours des angioplas-

ties. Cependant, cet outil d'une très grande richesse devrait devenir le « compagnon » indispensable de tout angioplasticien et devrait donc être présent dans tous les laboratoires de cathétérisme. Effectivement, l'échographie endovasculaire pourrait être comparée à « l'œil de l'anatomopathologiste » tant il est vrai que les informations apportées sont comparables à celles du pathologiste dans leur précision et dans leur justesse d'observation. L'angiographie coronaire est d'interprétation quelquefois difficile et parfois ambiguë : il est alors nécessaire d'utiliser cette technique complémentaire pour redresser notre interprétation angiographique tout en améliorant nos interprétations angiographiques avec un *gold standard* anatomique.

MOTS CLÉS : échographie endovasculaire, stent, angioplastie, remodelage artériel, athérosclérose.

Références

1. Finet G, Moll T, Tabib A et al. Analyse par les courbes ROC des performances d'interprétation en échographie endovasculaire. Arch Mal Cœur 1997 ; 90 : 59-66.
2. Finet G, Maurincomme E, Reiber JHC, Savalle L, Magnin I, Beaune J. Evaluation of an automatic intraluminal edge detection technique for intravascular ultrasound images. Japanese Circ J 1997 ; 62 : 117-25.
3. Cachard C, Finet G, Bouakaz A, Tabib A, Francon D, Gimenez G. Ultrasound contrast agent in intravascular echography. Ultrasound Med Biol 1997 ; 23 : 705-17.
4. Mehran R, Mintz GS, Hong MK et al. Validation of the in vivo intravascular ultrasound measurement of in-stent neointimal hyperplasia volumes. J Am Coll Cardiol 1998 ; 32 : 794-9.
5. Maurincomme E, Magnin IE, Finet G, Goutte R. Methodology for three-dimensional reconstruction in intravascular ultrasound images. In Kim Y (ed). proceeding of the Medical Imaging VI: Image Capture, Formatting, and Display. Vol. SPIE 1653 , 1992 : 26-34.
6. Finet G, Maurincomme E, Douek Ph, Tabib A, Amiel M, Beaune J. Three-layer appearance of the arterial wall in intravascular ultrasound imaging: artifact or reality? Implications for accurate measurements in quantitative intravascular ultrasound. Echocardiography 1994 ; 11 : 343-63.
7. Finet G, Douek P, Tabib A et al. L'imagerie échographique endovasculaire : revue des applications et des limitations. A propos d'une étude in vitro. Arch Mal Cœur 1993 ; 86 : 1371-81.
8. Nakamura S, Colombo A, Gaglione A et al. Intracoronary ultrasound observations during stent implantation. Circulation 1994 ; 89 : 2026-34.
9. Görge G, Haude M,. Ge J et al. Intravascular ultrasound after low and high inflation pressure coronary artery stent implantation. J Am Coll Cardiol 1995 ; 26 : 725-30.
10. Di Mario C, Görge G, Peters R et al. Clinical application and image interpretation in intracoronary ultrasound. European Heart Journal 1998 ; 19 : 207-29.
11. Slepian MJ. Application of intraluminal ultrasound imaging to vascular stenting. Int J Card Imaging 1991 ; 6 : 285-311.
12. Finet G, Dayoub G, Boschat J et al. Description of different atherosclerosis stenosis patterns by intravascular ultrasound. Eur Heart J 1997 ; 18 (suppl.) : 615.
13. Delachartre Ph, Cachard C, Finet G, Gerfault L, Vray D. Modelling geometric artefacts in intravascular ultrasound imaging. Ultrasound Med Biol 1999 ; 25 : 567-75.
14. Abizaid A, Mintz GS, Pichard AD et al. Is intravascular ultrasound clinically useful or is it just a research tool? Heart 1997 ; 78 (suppl. 2) : 27-30.
15. Finet G, Lienard J. Optimizing coronary angiography views. Int J Cardiac Imaging 1996 ; 11 : 53-4.
16. Glagov S, Weisenberg E, Zarins CK, Stankunavicius R, Kolettis GJ. Compensatory enlargement of human atherosclerotic coronary arteries. N Engl J Med 1987 ; 316: 1371-5.

17. Mintz GS, Kent KM, Pichard AD, Satler LF, Popma JJ, Leon MB. Contribution of inadequate arterial remodeling to the development of focal coronary artery stenoses. An intravascular ultrasound study. Circulation 1997 ; 95 : 1791-8.
18. Lafont A, Guzman LA, Whitlow PL, Goormastic M, Cornhill JF, Chisolm GM. Restenosis after experimental angioplasty. Intimal, medial, and adventitial changes associated with constrictive remodeling. Circulation 1995 ; 76 : 996-02
19. Rioufol G, Finet G, Tabib A, Beaune J. The (often) four-layer apparence of coronary arteries by intravascular ultrasound: the tunica adventitia. J Am Coll Cardiol 1999 ; abstract 77 A.
20. Finet G, Tabib A, Douek P et al. Imagerie échographique endovasculaire : validations expérimentales et limitations. Arch Mal Cœur 1993 ; 86 : 1373-81.
21. Lee DY, Eigler N, Luo H et al. Effect of intracoronary ultrasound imaging on clinical decision making. Am Heart J 1995 ; 129 : 1084-93.
22. Mintz GS, Popma JJ, Hong MK et al. Intravascular ultrasound to discern device-specific effects and mechanisms of restenosis. Am J Cardiol 1996 ; 78 (suppl. 3A) : 18-22.
23. Görge G, Ge J, Haude M et al. Intravascular ultrasound: a guide for management of complications during intervention. European Heart Journal 1995 ; 16 (suppl. L) : 86-92.
24. Stone GW, Hodgson JM, St Goar FG et al. Improved procedural results of coronary angioplasty with intravascular ultrasound-guided balloon sizing. The CLOUT pilot trial. Circulation 1997 ; 95 : 2044-52.
25. Mu dra H, Werner F, Regar E et al. One balloon approach for optimized Palmaz-Schatz stent implantation: the MUSCAT trial. Cathet Cardiovasc Diagn 1997 ; 42 : 130-6.
26. Jain SP, Jain A, Collins TJ, Ramee SR, White CJ. Predictors of restenosis: a morphometric and quantitative evaluation by intravascular ultrasound. Am Heart J 1994 ; 128 : 664-73.
27. Schroeder S, Baumbach A, Haase KK et al. Reduction of restenosis by vessel size adapted percutaneous transluminal coronary angioplasty using intravascular ultrasound. Am J Cardiol 1999 ; 83 : 875-9.
28. Bruining N, Sabaté M, Serruys PW. Clinical implications of intravascular ultrasound imaging for stenting procedures. Am Heart J 1999 ; 137 : 207-10.
29. Tobis JM, Colombo A. Do you need IVUS guidance for coronary stent deployment? Cathet Cardiovasc Diagn 1996 ; 37 : 360-1.
30. Etave F, Boivin M, Finet G, Boyer JC, Beaune J. Détermination des propriétés mécaniques des endoprothèses coronaires par l'utilisation des éléments finis. Arch Physiol Bio 1998 ; (suppl. II) : 106-9.
31. Schiele F, Meneveau N, Vuillemot A et al. Impact of intravascular ultrasound guidance in stent deployment on 6-month restenosis rate: a multicenter, randomized study comparing two strategies-with and without intravascular ultrasound guidance. J Am Coll Cardiol 1998 ; 32 : 320-8.

NSDOCID: <XP___1014246A__I_>